

# UCLA

## UCLA Previously Published Works

### Title

Laboratory-numerical models of rapidly rotating convection in planetary cores

### Permalink

<https://escholarship.org/uc/item/1zb249hs>

### Journal

Geophysical Journal International, 201(1)

### ISSN

0956-540X

### Authors

Cheng, JS  
Stellmach, S  
Ribeiro, A  
et al.

### Publication Date

2015

### DOI

10.1093/gji/ggu480

Peer reviewed

# Laboratory-numerical models of rapidly rotating convection in planetary cores

J. S. Cheng,<sup>1</sup> S. Stellmach,<sup>2</sup> A. Ribeiro,<sup>1</sup> A. Grannan,<sup>1</sup> E. M. King<sup>3</sup> and J. M. Aurnou<sup>1</sup>

<sup>1</sup>Department of Earth, Planetary and Space Sciences, University of California - Los Angeles, CA, USA. E-mail: [j.shuo.cheng@gmail.com](mailto:j.shuo.cheng@gmail.com)

<sup>2</sup>Institut für Geophysik, WWU Münster, Münster, Germany

<sup>3</sup>Miller Institute and Department of Earth and Planetary Science, Berkeley, CA, USA

Accepted 2014 December 11. Received 2014 October 20; in original form 2014 May 21

## SUMMARY

We present laboratory and numerical models investigating the behavioural regimes of rapidly rotating convection in high-latitude planetary core-style settings. Our combined laboratory-numerical approach, utilizing simplified geometries, can access more extreme parameters (e.g. Rayleigh numbers  $Ra \lesssim 10^{13}$ ; Nusselt numbers  $Nu \lesssim 10^3$ ; Ekman numbers  $E \gtrsim 3 \times 10^{-8}$ ) than current global-scale dynamo simulations. Using flow visualizations and heat transfer measurements, we study the axialized flows that exist near the onset of rotating convection, as well as the 3-D flows that develop with stronger forcing. With water as the working fluid (Prandtl number  $Pr \simeq 7$ ), we find a steep scaling trend for rapidly rotating convective heat transfer,  $Nu \sim (Ra/Ra_C)^{3.6}$ , that is associated with the existence of coherent, axialized columns. This rapidly rotating trend is steeper than the trends found at moderate values of the Ekman number, and continues a trend of ever-steepening scalings as the rotation rate of the system is increased. In contrast, in more strongly forced or lower rotation rate cases, the heat transfer scaling consistently follows a shallower slope equivalent to that of non-rotating convection systems. The steep heat transfer scaling in the columnar convection regime, corroborated by our laboratory flow visualizations, imply that coherent, axial columns have a relatively narrow range of stability. Thus, we hypothesize that coherent convection columns are not stable in planetary core settings, where the Ekman number is estimated to be  $\sim 10^{-15}$ . As a consequence, convective motions in the core may not be related to the columnar motions found in present-day global-scale models. Instead, we hypothesize that turbulent rotating convection cascades energy upwards from 3-D motions to large-scale quasi-2-D flow structures that are capable of efficiently generating planetary-scale magnetic fields. We argue that the turbulent regimes of rapidly rotating convection are essential aspects of core dynamics and will be necessary components of robust, next-generation and multiscale dynamo models.

**Key words:** Dynamo: theories and simulations; Heat flow; Core, outer core and inner core; Planetary interiors.

## 1 INTRODUCTION

In the investigation of planetary core physics, the current methodological paradigm depends primarily upon numerical dynamo models. These models strive to simulate the global scale processes occurring in planetary interiors by solving the governing equations of magnetohydrodynamic flow in a rotating spherical shell of electrically conductive fluid (e.g. Kageyama & Sato 1995; Glatzmaier & Roberts 1996; Christensen & Aubert 2006). The strength of these models is that they are capable of reproducing some major features of the geomagnetic field, including the dipolar morphology, flux patches at high latitudes and polarity reversals (e.g. Christensen 2010; Olson *et al.* 2011).

However, these models are limited because they require overly strong viscous diffusive effects. Over 10 orders of magnitude larger than estimates for Earth's core, the viscous diffusion in current numerical dynamo models ultimately removes all but the largest scale motions in the system (e.g. Soderlund *et al.* 2012). Small-scale turbulence and turbulent fluxes between large- and small-scale processes cannot exist in these models (*cf.* Braginsky & Meytlis 1990). As such, the models are effectively laminar. However, turbulent fluid systems, such as exist in planetary cores, are inherently multiscale: a wide range of flow scales are expected to be active and interrelated (Nataf & Schaeffer 2015). For example, convective energy is likely injected at very small scales into the core fluid, whereas magnetic fields are likely generated by larger-scale flows. In the long term, in

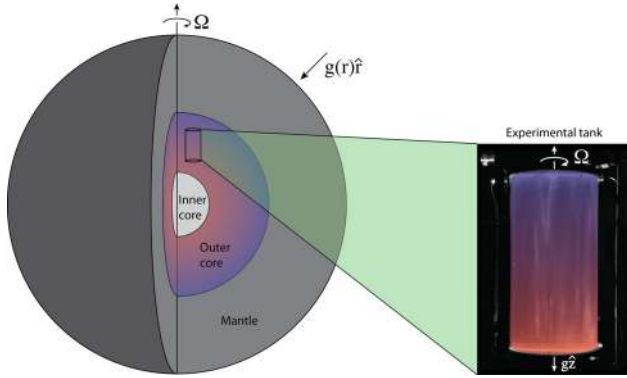


**Figure 1.** Image showing the conceptual relationship between a parcel of core fluid and our laboratory rotating convection experiments. Gravitational acceleration is represented by  $g$  and the angular rotation vector is represented by  $\Omega$ . In addition, the adverse density gradient is qualitatively represented by the background colour scheme. Violet represents higher density fluid while pink represents lower density fluid.

order to make accurate predictions of global scale observables, we must understand the path by which small-scale convective energy is transferred to the large-scale flows that effectively induce magnetic fields.

To investigate the behaviour of rapidly rotating convection toward the limit of core-style turbulence, we have used laboratory simulations of rapidly rotating convection and high-resolution numerical models in a complementary fashion. Here we present the results of the combined approaches, which have allowed us to access the axialized flows that exist near the onset of convection, as well as the 3-D turbulent flows that develop with stronger forcing. Together our combined laboratory-numerical approach provides a broad view of the regimes that likely describe core-style rotating convective motions. We do not include the effects of magnetic fields on convection (*cf.* Cioni *et al.* 2000; Aurnou & Olson 2001; Stellmach & Hansen 2004; Gillet *et al.* 2007; Hori *et al.* 2010; King & Aurnou 2015; Ribeiro *et al.* 2015). In addition, we use simplified geometries. Right cylinders are used in the laboratory experiments and Cartesian domains are used in the numerical simulations, both of which remove the effects of spherical shell curvature (see Fig. 1). In these reduced geometries, we are able to reach more extreme parameter values than are accessible in current global-scale dynamo models.

Our study then differs from the geophysical problem of rotating magnetoconvection in a spherical shell. However, understanding the reduced problem serves as an essential prerequisite to understanding planetary convection. In addition, our systematic approach provides the opportunity to contextualize core fluid dynamics, using the predictions derived in the well-established body of convection physics literature (e.g. Malkus 1954; Kraichnan 1962; Julien *et al.* 1996; Grossmann & Lohse 2000; Sprague *et al.* 2006; Ahlers *et al.* 2009; Grooms & Whitehead 2015).

In the next section of this paper, we introduce the non-dimensional parameters necessary to discuss the theoretically predicted behaviours of (non-rotating) Rayleigh-Bénard convection and rotating convection. These simplified systems articulate the underlying physical processes that are the basis of all convectively driven dynamo models. In Section 3, we present our laboratory and numerical set-ups, with which we make detailed measurements of the convective heat transfer across a fluid layer and qualitative measurements of the associated flow patterns. Our results are provided

in Section 4. In Section 5, we discuss the regime transitions that exist in our heat transfer data, which provide important insight about rotating convection systems: we find that axially invariant rotating convection columns exist only over a very limited range of parameter space. In Section 6, we consider the extrapolation of our results to planetary core settings. Finally, in Section 7, we discuss how our findings better tie next-generation dynamo modelling results to established theories of turbulent convection.

## 2 SYSTEM PARAMETERS AND SCALING BEHAVIOURS

### 2.1 Rayleigh-Bénard convection (RBC)

In order to investigate rotating convection systems, we first consider the analogous non-rotating system. This non-rotating style of convection, known as RBC, describes the thermally induced overturning of fluid in a plane layer geometry. Non-rotating convection is relevant to planetary systems because it represents the limiting behaviour when convection overcomes rotational effects. We find that convective heat transfer in RBC systems provides upper bounding values on those that will be observed in rotating convection systems.

The effective strength of the thermal buoyancy force in RBC systems is denoted by the Rayleigh number. This non-dimensional number represents the ratio between thermally induced buoyancy and the viscous and thermal diffusive effects:

$$Ra = \frac{\text{Buoyancy}}{\text{Diffusion}} = \frac{\gamma g \Delta T L^3}{\nu \kappa}, \quad (1)$$

where  $\gamma$  is the thermal expansivity,  $g$  is gravitational acceleration,  $\Delta T$  is the temperature difference between the top and bottom horizontal boundaries of the fluid layer,  $L$  is the distance between these boundaries,  $\nu$  is the viscous diffusivity and  $\kappa$  is the thermal diffusivity. At a sufficiently high value of  $Ra$ , denoted as the critical Rayleigh number  $Ra_C$ , buoyancy effects overcome diffusion and the fluid layer becomes unstable to convective fluid motions. For an infinite plane layer with rigid, non-slip boundaries, the critical Rayleigh number in RBC has a constant value of  $Ra_C = 1708$  (Pellew & Southwell 1940).

The other parameter describing RBC systems is the thermal Prandtl number,  $Pr$ . This number is the ratio of the thermal and viscous diffusion timescales in the system,

$$Pr = \frac{\nu}{\kappa}, \quad (2)$$

and, thus, describes the thermophysical properties of the working fluid. For instance, in water, the working fluid used in our laboratory experiments,  $Pr$  has a value of  $\simeq 7$ . Present-day dynamo studies typically use a Prandtl number of  $\simeq 1$  (e.g. Olson *et al.* 2011; Soderlund *et al.* 2013). In contrast, it is estimated that the  $Pr \sim 10^{-2}$  in the liquid metal that makes up Earth's outer core (e.g. de Koker *et al.* 2012; Pozzo *et al.* 2012).

For any given set of  $Ra$  and  $Pr$  input parameters in an RBC system, the non-dimensional heat transfer is expressed in terms of the Nusselt number,  $Nu$ . The Nusselt number is the ratio of the total heat flux through the system normalized by the conductive heat flux in the absence of convection:

$$Nu = \frac{\text{Total heat flux}}{\text{Conductive heat flux}} = \frac{qL}{k\Delta T}, \quad (3)$$

where  $q$  is the total heat flux and  $k$  is the working fluid's thermal conductivity. Because the total (superadiabatic) heat flux is the

sum of convective and conductive components, the Nusselt number will have a fixed value of unity in the absence of convective motions, and will reach higher values as the convective heat flux increases in strength. (Unlike in planets, the adiabatic heat flux is zero in our experiments.) In our laboratory-numerical RBC experiments, the Nusselt number ranges from values of unity to just over  $10^3$ , demonstrating that we can study the full range of behaviours that exist between the onset of convection and fully developed, convection-dominated heat transfer.

The Nusselt number provides a globally integrated description of the vigour of convective motions. As such, trends in the Nusselt number reveal fundamental behaviours of the underlying convection system (e.g. Spiegel 1971; Glazier *et al.* 1999). In the literature on convective turbulence, heat transfer in RBC systems follows several well known scaling laws of the form  $Nu \sim Ra^\alpha Pr^\chi$  (e.g. Ahlers *et al.* 2009). However, since we use a fixed Prandtl number in our experiments, we will consider RBC scalings of the simpler form

$$Nu = c_1 Ra^\alpha, \quad (4)$$

where  $c_1$  is the pre-factor and  $\alpha$  is the scaling exponent. Such scalings have been predicted theoretically and confirmed experimentally over wide ranges of parameter space (e.g. Rossby 1969; Castaing *et al.* 1989; Glazier *et al.* 1999; Funfschilling *et al.* 2005).

There are two well-known  $Nu \sim Ra^\alpha$  scaling regimes of RBC heat transfer that are accessible with our experiments. One classical prediction, first theorized by Malkus (1954), is the  $\alpha = 1/3$  relation. Malkus' arguments apply to systems containing vigorous convective mixing, where the bulk fluid becomes isothermal and the time-averaged temperature gradients are localized to thin thermal boundary layers adjacent to the top and bottom of the fluid layer. Conductive heat transport dominates in these quasi-static boundary layers. The  $\alpha = 1/3$  law arises under conditions in which the opposing boundary layers do not interact, and the fluid layer height therefore does not enter into the heat transfer scaling. This depth-independent heat transfer then leads to the following scaling law:

$$Nu \sim (Ra/Ra_C)^{1/3}. \quad (5)$$

This scaling law has been verified in a number of experiments carried out at  $Ra \gtrsim 10^{10}$  (Ahlers *et al.* 2009). It is often argued that the  $\alpha = 1/3$  law is appropriate for geophysical systems in which the boundary layers act in relative isolation, such as when they are much thinner than the total thickness of the fluid layer (e.g. Castaing *et al.* 1989).

In RBC laboratory and numerical experiments at moderate buoyancy forcings ( $Ra \lesssim 10^{10}$ ), characteristic of values used in current-day dynamo models, the  $\alpha = 1/3$  law is not typically observed. Instead, experiments in this moderate  $Ra$  range find that the RBC heat transfer follows a law closer to  $Nu \sim Ra^{2/7}$  (Chillá *et al.* 1993; Glazier *et al.* 1999; Ahlers & Xu 2001). In most  $Ra \gtrsim 10^5$  laboratory and numerical experiments, a container scale overturning circulation occurs in the bulk fluid, providing a shear flow across the boundaries. The presence of this circulation implies communication between the boundary layers and that the depth of the fluid layer is a critical characteristic of the system. By including the effects of a shear flow across the thermal boundary layers, Shraiman & Siggia (1990) argue that an  $\alpha = 2/7$  heat transfer scaling develops.

At extremely high  $Ra$ , which presently exceed laboratory and numerical experimental capabilities, an  $\alpha = 1/2$  scaling law has been hypothesized (Kraichnan 1962; Spiegel 1971). In this regime, the thermal boundary layers become fully turbulent. In the absence of quasi-static boundary layers, the heat flux will be controlled

solely by turbulent flows occurring within the fluid bulk and the microscopic, molecular properties of the fluid may cease to play a role. This RBC heat transfer regime is represented by the scaling law

$$Nu \sim (Ra Pr)^{1/2}. \quad (6)$$

Although this scaling has yet to be observed experimentally (e.g. Roche *et al.* 2010), it may ultimately apply to buoyancy-dominated planetary and astrophysical convection systems. In our present laboratory and numerical experiments, we are able to access the  $\alpha \simeq 2/7$  and  $1/3$  regimes.

## 2.2 Rotating convection

With the inclusion of rotation in a given system, new modes of convection can develop, associated with alternate regimes of convective heat transfer. A new non-dimensional parameter, the Ekman number  $E$ , is required to characterize the effect of the system's rotation. This parameter is defined by the ratio between the system-scale viscous force and the Coriolis force:

$$E = \frac{\text{Viscosity}}{\text{Coriolis}} = \frac{\nu}{2\Omega L^2}, \quad (7)$$

where  $\Omega$  is the system's angular rotation rate. In many geophysical settings, the Ekman number is extremely small, implying that rotational effects massively overwhelm global-scale viscous forces. For instance, the Ekman number is estimated to be of order  $10^{-15}$  in Earth's core (Schubert & Soderlund 2011). At such low values, the system-scale flows are expected to be essentially unaffected by fluid viscosity (e.g. Roberts & King 2013).

The effect of rotation is strongly constraining and has the effect of suppressing the onset of convection (e.g. Nakagawa & Frenzen 1955). The critical Rayleigh number in a rotating convection system is no longer a constant for a given geometry. Instead,  $Ra_C$  grows with the system's rotation rate:

$$Ra_C = c_2 E^{-4/3}, \quad (8)$$

where  $c_2$  is 8.696 for the onset of steady rotating convection as  $E \rightarrow 0$  (Chandrasekhar 1961). At the onset of rotating convection, fluid motions occur in the form of long, thin columns that are aligned with the rotation axis (Grooms *et al.* 2010; King & Aurnou 2012). The narrow horizontal width of these columns,  $\ell$ , results in viscous forces that locally relax the rotational constraint on fluid flow. The width of the columns at the onset of convection scales as:

$$\ell = c_3 E^{1/3} L, \quad (9)$$

where  $c_3 = 4.8$  as  $E \rightarrow 0$  (e.g. Julien & Knobloch 1998). This  $E^{1/3}$  scaling result appears to hold well past onset and thus likely characterizes flow scales in a broad array of rapidly rotating convection settings (e.g. Zhang & Schubert 2000; Stellmach & Hansen 2004; King & Buffett 2013).

In spheres and spherical shells (with inner radius less than 3/4 of the outer shell radius), most of the fluid volume exists outside of the tangent cylinder. These lower latitude convection columns are generated by thermal Rossby waves and are not fully equivalent to our Cartesian cases, which better simulate convection at higher latitudes within the tangent cylinder (e.g. Busse & Cuong 1977; Sreenivasan & Jones 2006a; Takehiro 2008; Calkins *et al.* 2013). Because the vorticity changes sign across the mid-layer only in high latitude columns, they have differing topologies (Chandrasekhar 1961), differing heat transfer behaviours (e.g. Aurnou *et al.* 2007) and their vortex–vortex interactions are likely different. However,

they have some important similarities. In particular, they represent strongly axialized vortices that have  $\ell = O(E^{1/3})$  length scales (Zhang & Schubert 2000; King & Buffett 2013).

The vast majority of planetary dynamo models are carried out in the vicinity of  $E \sim 10^{-4}$  (King & Buffett 2013) where these axial columns, forming near the onset of convection, are the dominant flow structures. The columns in these models typically have widths that are large, in fact, close to the scale of the system,  $\ell/L \sim E^{1/3} \simeq 0.1$ , and have been argued to be an essential feature of Earth-like models (e.g. Christensen & Aubert 2006; Christensen 2010). The highly coherent axial flow structures are responsible for generating dipolar magnetic fields that are well aligned with the rotation axis. In fact, typical  $E \sim 10^{-4}$  models cannot generate Earth-like magnetic fields without the presence of axially coherent columns (e.g. Sreenivasan & Jones 2006b; Christensen 2010; Miyagoshi *et al.* 2010; Soderlund *et al.* 2012, 2013).

Even though dynamo models depend on columns as an essential building block, the width of those that exist in present-day models fundamentally differ from the columns that are presumed to exist in the core. For instance, in Earth's core, columns are not predicted to be the system-scale in width, but instead are likely to be extremely narrow with  $\ell/L \sim E^{1/3} \simeq 10^{-5}$ . This corresponds to core columns of order 1000 km high by 10 m wide. It is unlikely that such structures can induce magnetic fields or remain stable under turbulent core conditions. Thus, lower  $E$  realizations of rotating convection are necessary to determine the stability range of columnar-style rotating convective flows as core-like parameters are approached. Furthermore, accurate models of global heat transfer (eventually, in spherical shell geometries) are also required in the regime in which coherent rotating convection columns exist. By comparing the heat flux estimates from a given planetary core, it should then be possible to infer whether coherent columns will stably exist in a given geophysical system (e.g. King & Aurnou 2012; Soderlund *et al.* 2014).

King *et al.* (2012) argue that boundary layer physics controls rotating convective heat transfer in water. By assuming that Malkus' (1954) marginal boundary layer arguments hold in a rapidly rotating system, they develop theoretical arguments predicting that rotating convective heat transfer scales steeply:

$$Nu = (Ra/Ra_C)^3. \quad (10)$$

This steep, cubic scaling (10) is argued to hold from near the onset of convection until the  $Ra$  value at which the thermal boundary layer becomes nested within the mechanical Ekman layer:

$$Ra_T \sim E^{-3/2}. \quad (11)$$

Furthermore, it is hypothesized that the columns will lose their axial coherency in the vicinity of  $Ra/Ra_T \sim 1$ . The  $Pr \simeq 7$ ,  $E \simeq 10^{-7}$  numerical experiments carried out in this study reach lower values of  $Ra/Ra_T$  than any previous studies and, thus, are the first to clearly test the King *et al.* (2012) predictions.

### 3 METHODS

Our investigation involves both laboratory experiments and numerical simulations of convection in non-rotating and rotating systems.

#### 3.1 Laboratory experiments

We perform RBC and rotating convection experiments in an axially aligned cylindrical container with water as the working fluid. The top

and bottom of the container are made of aluminum, which provides nearly isothermal boundary conditions in all our laboratory experiments. We maintain a Biot number  $Bi \leq 0.1$ , implying that thermal gradients in the boundaries are negligible compared to those in the fluid. The cylindrical sidewall is made of Reynolds Polymer acrylic, which has a low thermal conductivity of  $k = 0.19 \text{ W m}^{-1} \text{ K}^{-1}$  and is optically clear. The sidewall has a thickness of 0.635 cm and an inner diameter of 19 cm. We are able to vary the height of the container, here using 40, 80 or 160 cm tall sidewalls (Fig. 2). A brushless servomotor rotates the device at rates between 0 and 60 revolutions per minute (rpm).

The fluid layer is heated from below by a non-inductively wound, electrical resistance element that applies between 10 and 600 W of power. Following Rossby (1969), the experiment is cooled from above via a double-spiral wound heat exchanger maintained at a constant temperature by a precision thermal bath. Temperature measurements are made by 12 temperature sensors located within 2 mm of the top and bottom boundaries of the fluid layer, providing accurate measurement of the vertical temperature difference across the fluid layer,  $\Delta T$ . The minimum  $\Delta T$  that can be measured is approximately 0.25 K, which sets the minimum  $Ra$  that we can access with any given tank. The combination of applied heating power and resultant temperature drop measured across the fluid layer allows us to calculate the Nusselt and Rayleigh numbers for each experimental case.

These geometrically narrow tanks require careful treatment of potential thermal losses through the sidewalls. To minimize these losses, the temperature of the room is set as closely as possible to the mean temperature of the working fluid. Furthermore, the device is wrapped in a 10-cm-thick layer of Insulfrax insulation. The room and mean fluid temperatures are continually measured, allowing us to estimate horizontal conductive, convective and radiative heat losses from the device. For all cases above 30 W of input heating power, sidewall heat losses account for less than 5 percent of the total.

In every  $Nu$ – $Ra$  case, the experiment is allowed to equilibrate until the mean temperature on each thermal sensor does not change by more than  $\sim 1$  percent over the course of 2 hr. This process usually takes approximately 8–12 hr. We then collect data for 2–3 hr per case at a data rate of 10 samples per second.

A suite of experiments that omit the sidewall insulation has also been made in order to make qualitative optical characterizations of the flow fields in our experiments. Without sidewall insulation, it is possible to pass a vertical laser light sheet through the optically clear sidewalls. By seeding the working fluid with reflective Kalliroscope flakes, we are able to visualize the pattern of differential shear within the fluid. These patterns are recorded with the use of a digital camera situated in the laboratory frame.

#### 3.2 Numerical simulations

While laboratory experiments enable us to characterize rapidly rotating turbulent convection at high Rayleigh and low Ekman numbers ( $5 \lesssim Ra/Ra_C \lesssim 60$  at  $E = 10^{-7}$ ), our laboratory system cannot reach low enough  $Ra$  values to investigate the physics between  $Ra_C$  and  $Ra_T$  for  $E \lesssim 3 \times 10^{-4}$ . Numerical simulations, in contrast, allow us to study the behaviour of rotating convection at the low  $Ra$  values inaccessible in the laboratory. The combination of laboratory and numerical methods provides a complementary characterization of rotating convection physics, accessing the full range from weakly supercritical to fully turbulent flows.

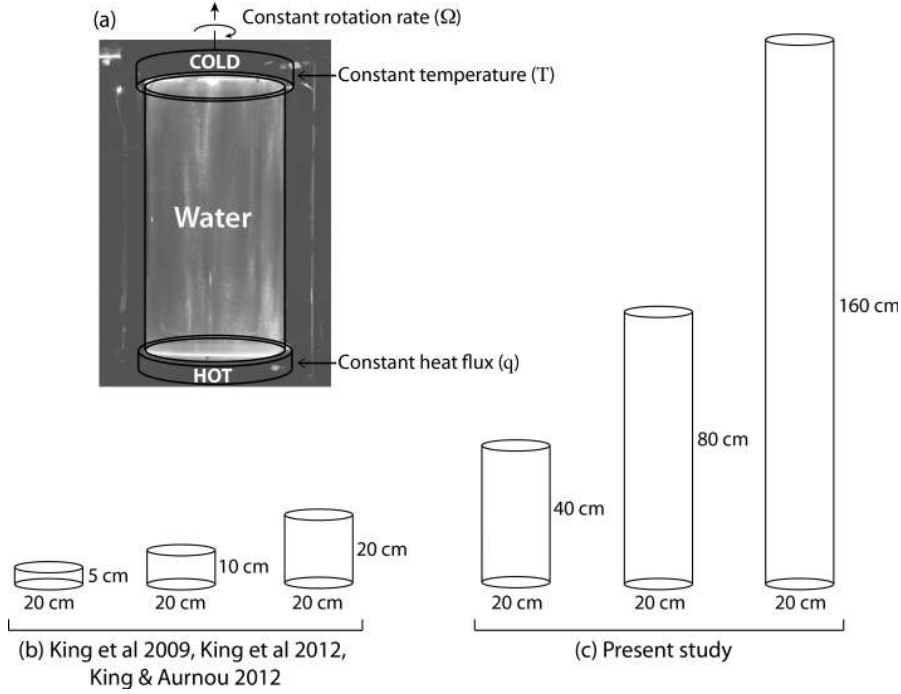


**Figure 2.** Experimental set-up: (a) a schematized image of the 40-cm-high by 20-cm-wide tank. An electrical heater provides a constant heat flux  $q$  to the base of the experiment. A water-cooled heat exchanger maintains a fixed temperature at the top of the system. A servomotor rotates the tank about a vertical axis at up to 60 revolutions per minute (rpm). All laboratory experiments have a fixed diameter of 20 cm. However, the heights of the tanks can be varied. (b) Preceding laboratory studies have employed 5, 10 and 20 cm high tanks (King *et al.* 2009, 2012; King & Aurnou 2012, 2013). (c) In this study, laboratory experiments are carried out in 40, 80 and 160 cm high tanks in order to reach more extreme ranges of parameter space. For example, in a 160-cm-high tank of water it is possible to attain  $E \gtrsim 3 \times 10^{-8}$  and  $Ra \lesssim 10^{13}$ .

The numerical models solve the Boussinesq momentum, energy and mass conservation equations in a rotating, Cartesian fluid layer. The top and bottom fluid layer boundaries are isothermal, rigid and non-slip. The solutions are periodic in the horizontal directions. Chebyshev polynomials are employed in the vertical direction and Fourier expansions in the horizontal directions. The vertical resolution is set in order to maintain at least 10 gridpoints within the Ekman boundary layer. The code has been validated in prior studies by Stellmach & Hansen (2008) and King *et al.* (2012).

## 4 RESULTS

Here, we briefly summarize our essential findings. First, we find in RBC experiments that a  $Nu-Ra$  scaling of  $\alpha = 0.284$  describes the heat transfer for  $Ra \lesssim 10^{10}$  and a scaling of  $\alpha = 0.322$  develops at roughly  $Ra \gtrsim 10^{10}$ , corresponding closely to the predicted 1/3 law. In rotating convection experiments, we find a steep heat transfer scaling law in the region where coherent convection columns exist. By comparing laboratory visualizations and heat transfer measurements, we show that this steep heat transfer scaling manifests when convection occurs in the form of axially invariant columns; when the columns become unstable to 3-D motions, the heat transfer becomes less efficient, trending back toward the non-rotating scaling. These results indicate that rotating convection columns, which form the conceptual underpinning for current Earth-like planetary dynamo models, exist only over a limited range of parameter space.

### 4.1 Laboratory flow visualizations

Fig. 3 shows Kalliroscope images of shear patterns in an 80-cm-high tank of convecting water for a fixed heating power of 10 W,

corresponding to a fixed flux-based Rayleigh number

$$Ra_F = Ra Nu = \frac{\gamma g L^4 q}{\rho C_p \kappa^2 \nu} = 4.0 \times 10^{12}. \quad (12)$$

In each experiment we test a different rate of rotation, ranging from 60 rpm down to 0 rpm. As the rotation rate is decreased, we see the organizing effect of Coriolis force weaken and give way to small-scale turbulence in the bulk fluid.

The image in Fig. 3(a), displaying a snapshot of the cylinder rotating at 60 rpm, shows the columnar convective regime. The strongly coherent columns extend between the bottom to the top boundary with almost no variation along the axial direction. Fig. 3(b) shows the flow field in a case rotating at 10 rpm ( $E = 7.5 \times 10^{-7}$ ). With this decrease in rotation rate, the columns become wavy and begin to lose their axial invariance. Fig. 3(c) shows the development of 3-D, anisotropic flows. Figs 3(d) and (e) show 3-D turbulence that appears to be isotropic in nature and is likely unaffected by rotation.

In addition, in Fig. 3, we estimate the strength of buoyancy effects for each of the five cases, but normalized in different ways. The first row gives the Rayleigh number normalized by the value at which bulk convection onsets,  $Ra/Ra_C$  (following eq. 8). The second row gives the Rayleigh number normalized by the boundary layer transition value,  $Ra_T$ , predicted in King *et al.* (2012). The third row gives the system-scale buoyancy force normalized by the Coriolis force, called the convective Rossby number  $Ro_c$ . The convective Rossby number can be written as:

$$Ro_c = \frac{\text{Buoyancy}}{\text{Coriolis}} = \left( \frac{Ra E^2}{Pr} \right)^{1/2}, \quad (13)$$

where the buoyancy and inertial terms have been set equal, and the inertial term can then be written in terms of the convective free-fall

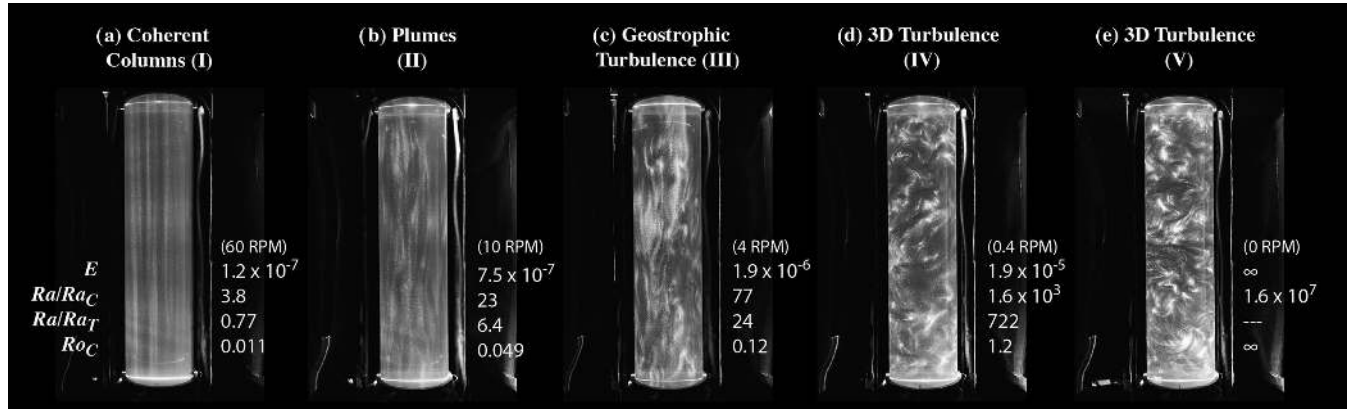


**Figure 3.** Laboratory visualizations of rotating convection in water at fixed heat flux. Panels (a) through (e) correspond to Ekman number values of  $E = 1.2 \times 10^{-7}$ ,  $7.5 \times 10^{-7}$ ,  $1.9 \times 10^{-6}$ ,  $1.9 \times 10^{-5}$  and  $\infty$ , respectively. All cases are carried out in an 80-cm-high by 20-cm-wide tank and at fixed flux Rayleigh number  $Ra_{F0} = 4.0 \times 10^{12}$ . Dimensionally, the rotation rates translate to 60, 10, 4, 0.4 and 0 revolutions per minute (rpm) and a constant heating power of 10 W. At  $E = 1.2 \times 10^{-7}$ , the flow is comprised of coherent, axialized convection columns. As  $E$  increases, the flow transitions to wavy plumes, then geostrophic turbulence, then homogenous turbulence (cf. Julien *et al.* 2012a, fig. 1). The  $Nu$ - $Ra$ - $E$  data from these visualization cases are demarcated by black-bordered yellow stars in heat transfer plots (Figs 4, 5 and 7), allowing us to qualitatively relate changes in flow morphology to changes in convective heat transfer regime. Movies corresponding to these cases can be found online at: [www.youtube.com/watch?v=p01r6l71ELA](http://www.youtube.com/watch?v=p01r6l71ELA).

velocity,  $U_f \sim \sqrt{y g \Delta T L}$ . The convective Rossby number is related to the modified Rayleigh number  $Ra^*$  defined in Christensen (2002) by  $Ro_C = Ra^*$ .

We argue that the case visualized in Fig. 3(c) corresponds to the geostrophic turbulence regime, where flows exhibit small-scale 3-D structure at convective Rossby number  $Ro_C \ll 1$  (cf. Sprague *et al.* 2006; Julien *et al.* 2012a). The flows in Figs 3(a)–(c), then, are in good agreement with the convective Taylor column, plume, and geostrophic turbulence regimes, respectively, found in asymptotically reduced rotating convection models of Julien *et al.* (2012a) and in direct numerical simulations conducted by Stellmach *et al.* (2014).

## 4.2 Rayleigh-Bénard convection

Fig. 4 shows RBC heat transfer data. The effective buoyancy force,  $Ra$ , is plotted on the  $x$ -axis; the resulting convective heat transfer,  $Nu$ , is plotted on the  $y$ -axis. Data from our 80 and 160 cm tall tank experiments are shown as purple-filled circles and diamonds, respectively, and are shown in comparison with data sets from previous RBC studies of Rossby (1969), Funfschilling *et al.* (2005) and King *et al.* (2012). The dashed green line

$$Nu = (0.162 \pm 0.006) Ra^{0.284 \pm 0.002} \quad (14)$$

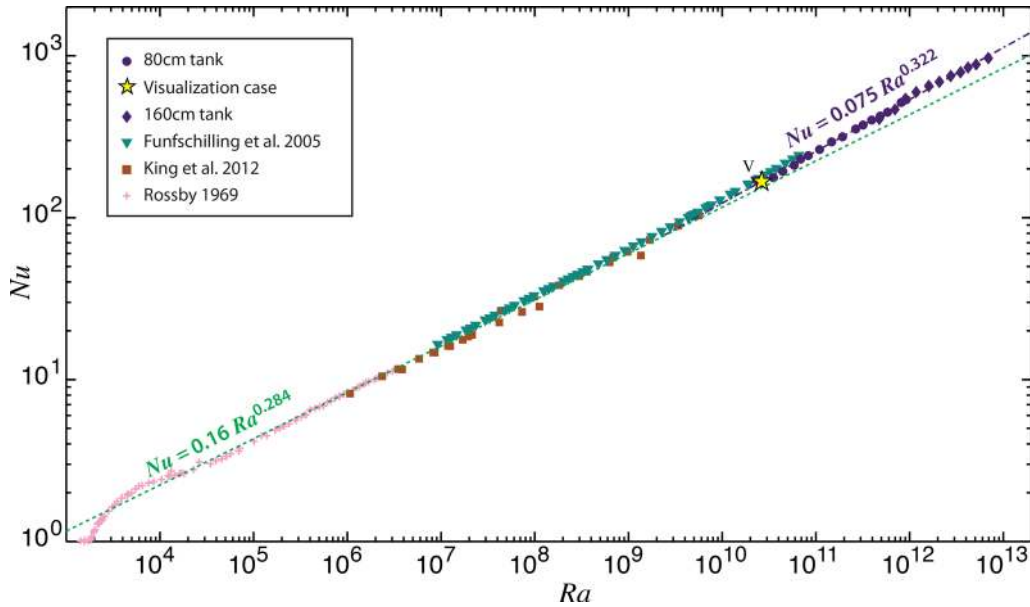


**Figure 4.** Laboratory Rayleigh-Bénard convection (RBC) heat transfer data alongside earlier data from Rossby (1969), Funfschilling *et al.* (2005) and King *et al.* (2012). The black-bordered yellow star denotes case V shown in Fig. 3, made at  $Ra_F = Nu Ra = 4 \times 10^{12}$ . For our present experiments ( $4 \lesssim Pr \lesssim 7$ ) in 80 and 160 cm tall tanks, the best-fitting heat transfer trend is  $Nu = (0.075 \pm 0.005) Ra^{0.322 \pm 0.003}$ , in approximate agreement with the theoretically predicted  $Nu \sim Ra^{1/3}$  law of Malkus (1954). At lower Rayleigh number experiments ( $4 \lesssim Pr \lesssim 10$ ) the best-fitting trend is  $Nu = (0.162 \pm 0.006) Ra^{0.284 \pm 0.002}$ , in agreement with the  $Nu \sim Ra^{2/7}$  law theorized in Shraiman & Siggia (1990) and observed in other laboratory experiments (e.g. Wu & Libchaber 1992; Chillá *et al.* 1993; Liu & Ecke 1997; Glazier *et al.* 1999).

is the best fit to the Rossby (1969) and King *et al.* (2012) data in the range  $10^5 < Ra < 10^{10}$ . This scaling exponent of  $\alpha = 0.284$  is in good agreement with a  $2/7$  law.

Beyond  $Ra = 10^{10}$ , the data from the 80 and 160 cm tanks and Funfschilling *et al.* (2005) rise more sharply than the  $\alpha \simeq 2/7$  green-dashed line. Instead, our 80 and 160 cm tank data then give a best-fitting scaling law of

$$Nu = (0.075 \pm 0.005)Ra^{0.322 \pm 0.003}, \quad (15)$$

which is statistically well outside the range of the  $2/7$  law, and in better agreement with Malkus' (1954)  $\alpha = 1/3$  law. This scaling is robust over several decades, from  $Ra \sim 10^{10}$  to  $10^{13}$ . Thus, we argue that the  $\alpha = 1/3$  law is affirmed in our laboratory RBC experiments.

### 4.3 Rotating convection

Fig. 5 shows rotating convection heat transfer data from our current laboratory and numerical experiments as well as the laboratory data from Rossby (1969) and the laboratory-numerical data from King *et al.* (2012). The colour coding denotes the Ekman number used in each experiment. Filled-in symbols indicate laboratory experiments, and open symbols indicate numerical simulations. The data show that, at each given rotation rate, convection onsets at different Rayleigh numbers, in good agreement with the prediction for the onset of convection in a rotating fluid layer (8). Once convection onsets,  $Nu$  increases more steeply with  $Ra$  than in non-rotating convection experiments (we refer to this steeper slope as  $\beta$ ). However, at high enough  $Ra$ , the rotating heat transfer data conforms to the non-rotating  $2/7$  scaling trend.

Thus, RBC scalings provide the effective upper bounds for heat transfer in rotating convection systems. The RBC heat transfer data acts as a ceiling, which the rotating heat transfer data either meets or falls beneath. There is a slight overshoot of rotating heat transfer beyond the RBC scalings for  $Ra \gtrsim Ra_T$  (*cf.* Niiler & Bisshopp

**Table 1.** Critical Rayleigh number estimates for no-slip boundaries, following Chandrasekhar (1961, section 27b).

$E$	$Ra_C$
$10^{-3}$	$7.159 \times 10^4$
$10^{-4}$	$1.544 \times 10^6$
$10^{-5}$	$3.482 \times 10^7$
$10^{-6}$	$7.825 \times 10^8$
$10^{-7}$	$1.741 \times 10^{10}$

1965; Julien *et al.* 1996; Kunnen *et al.* 2008). However, this effect is strong only at relatively high  $E$ . In fact, our data shows that the overshoot becomes small for  $E \lesssim 10^{-5}$ .

The slope of the steep scaling regime changes as a function of  $E$ . At the highest  $E$  values ( $E \simeq 10^{-3}$ ), the data conform to a  $\beta \simeq 6/5$  law (Christensen 2002; Aurnou 2007; King *et al.* 2009, 2010; Schmitz & Tilgner 2009). At lower  $E$  values in the vicinity of  $10^{-5}$ , the data fit a steeper, roughly cubic scaling law in agreement with King *et al.* (2012). However, for even more rapidly rotating cases, with data lying in the range  $10^{10} \lesssim Ra \lesssim 10^{11}$ , the best-fitting trend to the predominantly numerical  $E = 10^{-7}$  data is:

$$Nu = (0.71 \pm 0.09)(Ra/Ra_C)^{3.56 \pm 0.08}. \quad (16)$$

Here,  $Ra_C$  is estimated following Chandrasekhar (1961) (Table 1). This  $\beta \simeq 3.6$  trend is significantly steeper than any previous rotating convection experiments, exceeding even the cubic heat transfer scaling of King *et al.* (2012). Although we have carried out a limited number of numerical simulations in this low  $E$ , steep scaling regime, the best-fitting trend is statistically distinct from a cubic law. Julien *et al.* (2012b) argue that the  $\beta = 3$  law is among a family of plausible solutions for rapidly rotating convection, found to contain marginally unstable thermal boundary layers. However, our  $\beta = 3.6$  result implies that the marginal rotating boundary layer mechanism

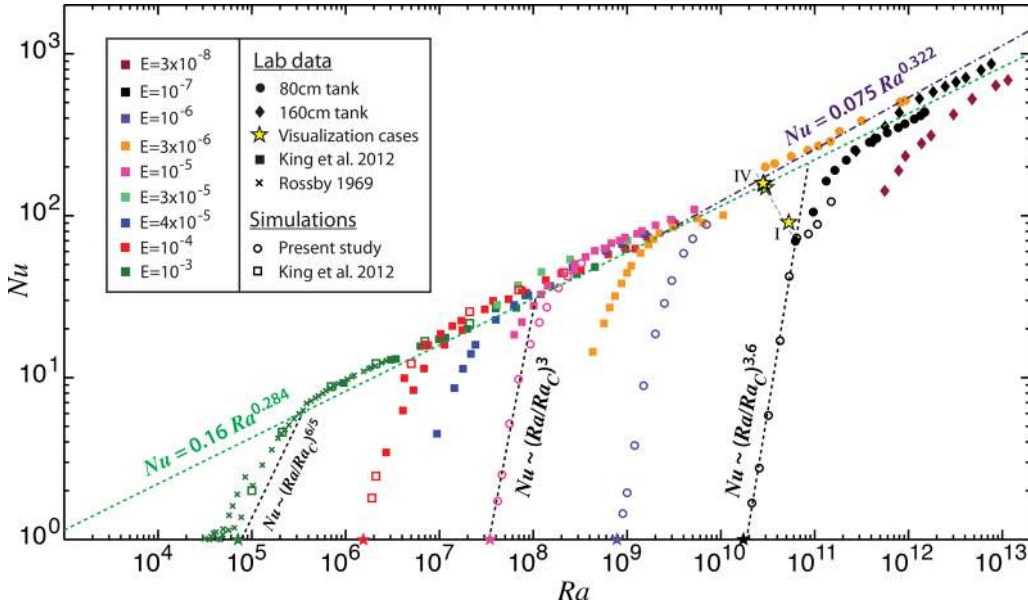


**Figure 5.** Laboratory ( $Pr \simeq 7$ ) and numerical ( $Pr = 7$ ) rotating convection heat transfer data from this study, Rossby (1969) and King *et al.* (2012). The black-bordered yellow stars denote cases I–IV shown in Fig. 3, made at fixed  $Ra_F = NuRa = 4 \times 10^{12}$ . This  $Ra_F$  value is denoted by the grey dashed line behind the stars. Critical Rayleigh number values from Table A2 are plotted as coloured stars along the  $x$ -axis. The best-fitting heat transfer trend of  $Nu \simeq (Ra/Ra_C)^{3.6}$  is plotted for  $E \sim 10^{-7}$ . For comparison,  $Nu = (Ra/Ra_C)^3$  (King *et al.* 2012) is plotted for  $E \sim 10^{-5}$  and  $Nu = (Ra/Ra_C)^{6/5}$  (King *et al.* 2009, 2010) for  $E \sim 10^{-3}$ . Note that with each study at lower  $E$ , the scaling exponent becomes larger. This implies that the behaviour of rotating convection is not yet asymptotic in the presently accessible range of  $Nu$ – $Ra$ – $E$  space.

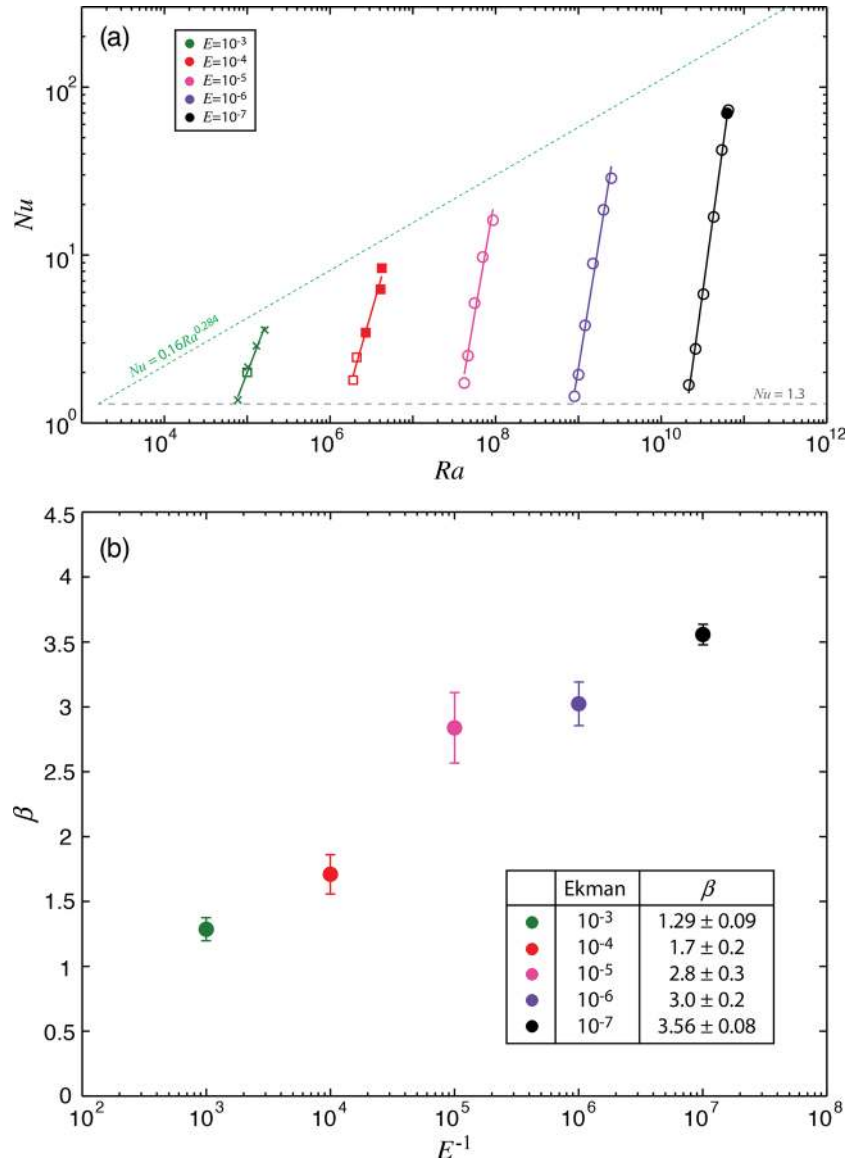


**Figure 6.** Heat transfer scaling exponents as a function of Ekman number. (a) Solid lines show the best-fitting  $Nu \sim Ra^\beta$  trends to combined laboratory and numerical data sets at  $E = 10^{-3}$ ,  $10^{-4}$ ,  $10^{-5}$ ,  $10^{-6}$  and  $10^{-7}$  in the steep heat transfer scaling regime. Data points used in the fits are selected to lie above  $Nu = 1.3$ , represented by the grey dashed line, and below the RBC trend of  $Nu = 0.16Ra^{0.284}$ , represented by the green dashed line. Symbols are as defined in Fig. 5. (b) Plot of  $\beta$  versus inverse  $E$  from the fits shown in panel (a). No clear asymptotic scaling behaviour has been found in our experiments: the values of  $\beta$  continually increases as a function of  $E^{-1}$  (cf. Julien *et al.* 2012b; Grooms & Whitehead 2015).

put forth in King *et al.* (2012) does not control the convective heat transfer at very low  $E$ . Clearly, though, the robustness of this  $\beta \simeq 3.6$  trend must be confirmed with more  $Ra \ll Ra_T$  data (see data Tables A1 and A2 in the Appendix).

Fig. 6 shows the best-fitting values for  $\beta$  as a function of the inverse Ekman number. Data points below  $Nu = 1.3$  are not considered in these fits, as they correspond to a shallower  $Nu$ – $Ra$  near onset (e.g. Julien *et al.* 2012b). For the steep scaling regime, we find that  $\beta$  monotonically increases with decreasing  $E$ , with a roughly linear trend between  $\log(E)$  and  $\beta$ . This suggests that in the presence of no-slip boundaries the heat transfer scaling will continue to steepen as  $E$  is further decreased towards geophysically realistic values (cf. Grooms & Whitehead 2015). Our heat transfer measurements show that no clear asymptotic behaviour has been found in the rapidly rotating, steep scaling regime.

In rotating convection experiments, we find a shallow RBC-style heat transfer scaling (independent of  $E$ ) with  $\alpha \simeq 2/7$  at our highest  $Ra$  values (cf. Liu & Ecke 1997). In contrast, we find an  $\alpha \simeq 1/3$  scaling in the RBC experiments for  $Ra \gtrsim 10^{10}$ . We postulate that this high  $Ra$  rotating  $2/7$  scaling is a byproduct of finite centrifugation effects in our present laboratory set-up. In our 80-cm-tank experiments, the Froude number, which is the ratio of centrifugal force and laboratory gravity,  $Fr = \Omega^2 r/g$ , is approximately 0.4 in the  $E \simeq 10^{-7}$  experiments. The strong centrifugal buoyancy in these cases likely drives a mean meridional circulation across the tank boundaries (e.g. Marques *et al.* 2007) which we argue modifies the heat transfer to a  $2/7$  scaling, in accordance with the arguments of Shraiman & Siggia (1990). To test this hypothesis, we doubled the height of the tank (160 cm) while fixing the Ekman number ( $E \simeq 10^{-7}$ ), which decreases the strength of centrifugation by a

factor of 16. This yields a Froude number of 0.025. In Fig. 5, we show that the highest  $Ra$  data in the 160 cm tank have higher  $Nu$  values that appear to be trending toward a  $1/3$  law. The effects of centrifugation will be studied in detail in a following suite of experiments.

In our rotating convection experiments, the RBC scaling—in particular, the  $2/7$  law—is observed to form the upper bound for heat transfer. Thus, the RBC and rotating convection (RC) scaling behaviours are deeply connected; knowledge of the RBC scalings is pertinent to our understanding of both systems. We hypothesize then that rotating convection and dynamo studies, carried out at sufficiently extreme parameter values, will also be able to access theoretically predicted regimes of behaviour (e.g. Soderlund *et al.* 2012). In particular, asymptotically reduced rotating convection models by Julien *et al.* (2012a) predict distinct heat transfer scalings corresponding to each of the regimes visualized in Figs 3(b)–(d). In our  $E \geq 3 \times 10^{-8}$  data, we can unambiguously detect a steep and a shallow  $Nu$ – $Ra$  scaling, but even lower values of  $E$  are required to differentiate the independent scalings for intermediate regimes (*cf.* Ecke & Niemela 2014).

## 5 COMPARING REGIME TRANSITION HYPOTHESES

Our rotating convective heat transfer data shows a clear transition from a steep scaling regime near the onset of convection to a shallower heat transfer scaling at strongly supercritical Rayleigh numbers. The data appears to deviate away from the steep scaling law near to where rotating convection columns lose their strong axial coherence. This is relevant to our understanding of present-day ( $E \sim 10^{-4}$ ) planetary dynamo models because Earth-like dipolar dynamo action has been shown to fail in the vicinity of the heat transfer transition in these models (King *et al.* 2012), where rotating convection columns also lose their axial coherence (Soderlund *et al.* 2012). Thus, we hypothesize that the heat transfer transition in our extreme rotating convection data will provide a proxy for behavioural transitions in more extreme dynamo models.

The transition Rayleigh number,  $Ra_T$ , is defined empirically here to be the intersection between the steep heat transfer scaling  $Nu = (Ra/Ra_C)^\beta$ , and the shallow, RBC-style scaling  $Nu = c_1 Ra^\alpha$ . Setting these heat transfer trends equal and using (8) yields:

$$Ra_T = c_1^{1/(\beta-\alpha)} Ra_C^{\beta/(\beta-\alpha)} = c_1^{1/(\beta-\alpha)} c_2^{\beta/(\beta-\alpha)} E^{4\beta/3(\alpha-\beta)}. \quad (17)$$

The supercriticality at which this transition occurs can then be written as:

$$\frac{Ra_T}{Ra_C} = c_1^{1/(\beta-\alpha)} c_2^{\alpha/(\beta-\alpha)} E^{4\alpha/3(\alpha-\beta)}. \quad (18)$$

By applying (17) to the best-fitting scaling laws (15) and (16), we find:

$$Ra_T = (5.4 \pm 0.1) E^{-1.466 \pm 0.005}. \quad (19)$$

The steep heat transfer scaling exponent  $\beta = 3.6$  differs from a cubic law by about 16 per cent. However, the exponent in  $Ra_T$  differs from (11) by only about 2 per cent. This small 2 per cent difference arises because of the limited range between  $Ra_C$  and  $Ra_T$ :

$$\frac{Ra_T}{Ra_C} = 144 E^{-0.14} \sim E^{-1/7} \quad (20)$$

at  $E = 10^{-7}$ . At presently accessible Ekman numbers, the  $\beta = 3.6$  slope and the cubic slope correspond to very similar intersections with the RBC trend. The weak  $E^{-1/7}$  dependence in (20)

also implies that the steep scaling regime occupies a limited range of parameter space even when extrapolated to planetary conditions.

In Fig. 7, we collapse the laboratory-numerical data from the present study and King *et al.* (2012) using the best-fit scaling for the majority of the non-rotating data, (14), to compensate the Nusselt number data on the  $y$ -axis and using our best-fitting transition scaling (19) to compensate the Rayleigh number on the  $x$ -axis. The mean Prandtl number in laboratory cases is 6.8 and the numerical cases employ a Prandtl number of 7. The black-bordered yellow stars correspond to the visualization cases shown in Fig. 3. The locations of the black-bordered yellow stars demonstrate that columnar flows are associated solely with the steep heat transfer scaling: only the  $E = 1.2 \times 10^{-7}$  visualization case (I) has a Rayleigh number value that is less than  $Ra_T$ . This shows, in our  $Pr \simeq 7$  experiments, that the efficiency of heat transfer greatly lessens and transitions over to the RBC scaling trend once convection columns lose their axial coherence.

In Fig. 8, we test the ability of a number of mechanistic (non-empirical) rotating convection transition hypotheses available in the literature to collapse our heat transfer data. In panel (a) of Fig. 8, the  $x$ -axis is normalized by the convective Rossby number (13). It has been argued that the convection regime dominated by rotation extends from the onset of rotating convection at  $Ra_C$  near to where the convective Rossby number is of order unity,  $Ro_c \lesssim 1$  (e.g. Gilman 1977; Aurnou *et al.* 2007; Zhong & Ahlers 2010; Gastine *et al.* 2013, 2014; Stevens *et al.* 2013). This predicts that the steep heat transfer scaling regime will extend over the range  $Ra_C \lesssim Ra \lesssim E^{-2} Pr$ . This Rayleigh number range has a width of  $\sim E^{-2/3} Pr$ . However, Fig. 8(a) shows that the  $Ro_c$  normalization greatly spreads our heat transfer data and, therefore, does not correctly define the transition. Our results from Fig. 7 instead imply that the steep scaling regime—where we find that columns are stable—is a factor of  $\sim E^{3/5}$  narrower than the  $Ro_c \sim 1$  prediction.

It should be noted, however, that  $Ro_c \sim 1$  does provide an adequate transition prediction for zonal flow behaviour in rotating spherical shells because these flows occur on the system's global scale (e.g. Aurnou 2007; Gastine *et al.* 2013, 2014). However, in our rotating convection experiments, in which convective heat transfer is controlled by distinctly smaller scale motions, the data are not well collapsed by this system-scale parameter.

Fig. 8(b) shows a test of the *local* convective Rossby number,  $Ro_\ell$ . This parameter has been proposed in a number of previous dynamo studies (e.g. Christensen & Aubert 2006; Sreenivasan & Jones 2006b) to control the transition between dipolar and multipolar magnetic field generation, with a critical value of  $Ro_\ell \simeq 0.1$ . Here we write  $Ro_\ell$  as

$$Ro_\ell = \frac{U}{2\Omega\ell} = \frac{UL}{\nu} \frac{\nu}{2\Omega L^2} \frac{L}{\ell} = Re E \frac{L}{\ell}, \quad (21)$$

where the Reynolds number,  $Re$ , is defined as:

$$Re = \frac{\text{Inertia}}{\text{Viscosity}} = \frac{UL}{\nu}. \quad (22)$$

We cannot directly measure velocities in our laboratory experiments. In order, then, to express the local Rossby number in terms of our heat transfer data, we must make two assumptions. First, we replace  $L/\ell$  with  $(c_3 E^{1/3})^{-1}$  using (9), an approximation relevant to present-day dynamo studies following the arguments of King & Buffett (2013). Secondly, we give an approximate value of

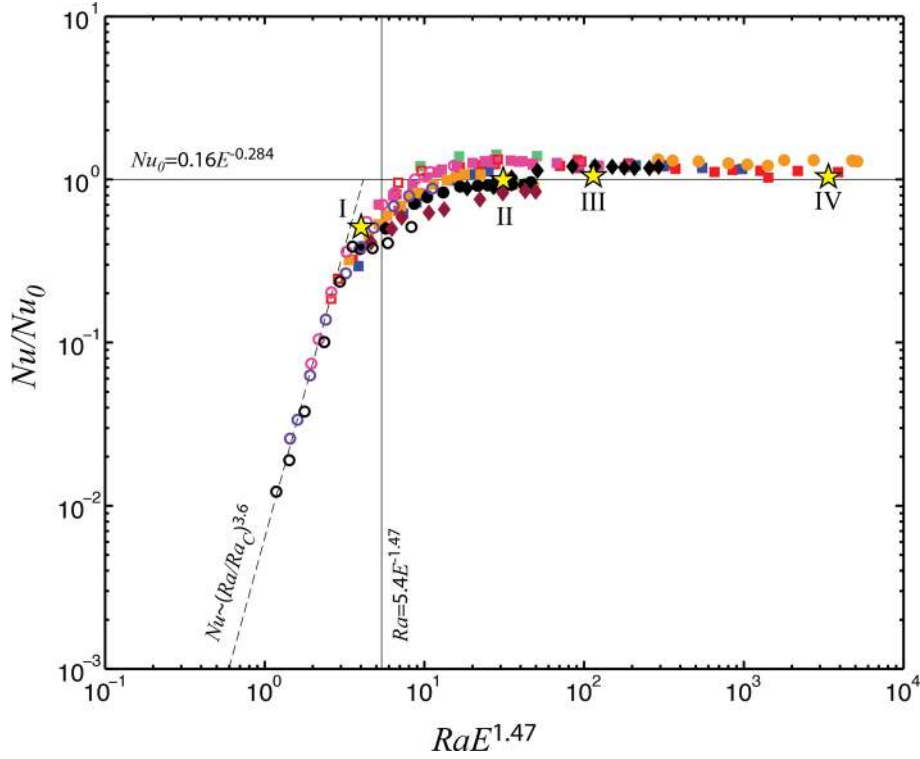


**Figure 7.** Test of the heat transfer transition argument based on our most extreme data. Data are from laboratory ( $Pr \simeq 7$ ) and numerical ( $Pr = 7$ ) rotating convection experiments with  $E \leq 10^{-4}$ . Symbols are as defined in Fig. 5. The y-axis is the non-dimensional heat transfer normalized by the non-rotating scaling  $Nu/Nu_0$ , where  $Nu_0 = 0.16Ra^{0.284}$  (14). The x-axis is the Rayleigh number normalized by the transition value  $Ra_T$ . This transition is empirically defined here as the intersection between the non-rotating heat transfer trend,  $Nu = 0.075Ra^{0.32}$ , and the rapidly rotating trend,  $Nu = 0.71(Ra/Ra_C)^{3.6}$ , and occurs at  $Ra_T = 5.4E^{-1.47}$  (19). The data from Fig. 3 have been included as black-bordered yellow stars in the collapse. These demonstrate that only the 60 rpm case (I) with coherent axial columns is found to plot within the steep heat transfer scaling regime.

the Reynolds number,  $\tilde{Re}$ , using the visco-Archimedean-Coriolis (VAC) second-order balance arguments in King *et al.* (2013):

$$\tilde{Re} = \frac{c_3(Nu - 1)^{1/2} Ra^{1/2} E^{1/3}}{Pr}. \quad (23)$$

Substituting  $\tilde{Re}$  into (21), gives

$$\tilde{Ro}_\ell = c_3^{-1} \tilde{Re} E^{2/3}. \quad (24)$$

We find that the  $Ro_\ell$  parametrization adequately collapses our  $Pr \simeq 7$  heat transfer data.

The inset in Fig. 8(b) tests another estimate for the local Rossby number,  $Ro_\ell^* = (\gamma g \Delta T)/(\Omega L^{1/2})$ , based on the free-fall velocity  $U_f$ . This estimate does not collapse the data as well as the  $Ro_\ell$  estimate derived from the VAC balance arguments presented in (23) and (24).

In Fig. 8(c), we test the transition arguments of King *et al.* (2009), which rely on the empirical  $Nu \sim (Ra/Ra_C)^{6/5}$  steep scaling regime and the  $Nu \sim Ra^{2/7}$  shallow scaling regime. The resulting transition scaling,  $Ra_T \sim E^{-7/4}$ , does not strongly collapse our present, lower  $E$  heat transfer data. However, the essential concept posited in King *et al.* (2009)—that boundary layer processes under the heat transfer transition—are not refuted (Niemela & Sreenivasan 2006; Cébron *et al.* 2010; Julien *et al.* 2012b).

Fig. 8(d) tests the  $Ra_T \sim E^{-3/2}$  transition argument from King *et al.* (2012). This transition parametrization collapses the data comparably well to that of Fig. 7. This agreement is expected since the present best-fit transition scaling and King *et al.*'s transition scaling differ only by a factor of  $\sim E^{1/50}$ .

In sum, there is great variance in the mechanistic arguments which seek to parametrize the behavioural regimes of rotating convective heat transfer, implying that our understanding of this system is still far from complete. Thus, further data sets that extend well below  $E = 10^{-7}$  are needed to determine an unambiguous, asymptotically robust, mechanistic transition argument that may be extrapolated to planetary conditions with confidence.

## 6 EXTRAPOLATION TO PLANETARY CORE SETTINGS

Our mixed heat transfer-visualization data, shown in Fig. 7, forms the basis of our assumption that axially coherent columns exist in rotating convection over the range  $Ra_C < Ra < Ra_T$ . Fig. 9 graphically represents this by plotting  $Ra_T/Ra_C$  as a function of inverse  $E$  for various transition scalings. Table 2 lists values of  $Ra_T$  and  $Ra_T/Ra_C$  extrapolated to  $E = 10^{-15}$ . The classical transition estimate of  $Ro_\ell \sim 1$  suggests that convection columns will be stable over 8 orders of magnitude in  $Ra$ . However, this scaling fails to meaningfully collapse the available data, as shown in Fig. 8. Our present results and other recent studies all estimate significantly smaller  $Ra_C < Ra < Ra_T$  ranges under which columns will be stable in the core. The  $Ra_T/Ra_C$  estimates in Table 2 show that, irrespective of the convection column breakdown mechanism, it is likely that traditional columns are unstable in core-like environments.

Fig. 10 displays, in the lower left-hand corner, all the rotating convection data from Fig. 5. On the right-hand side of the figure, we extrapolate our most extreme, steep heat transfer scaling,  $\beta = 3.6$ , from  $E = 10^{-7}$  to the typical estimate for the Ekman number in the

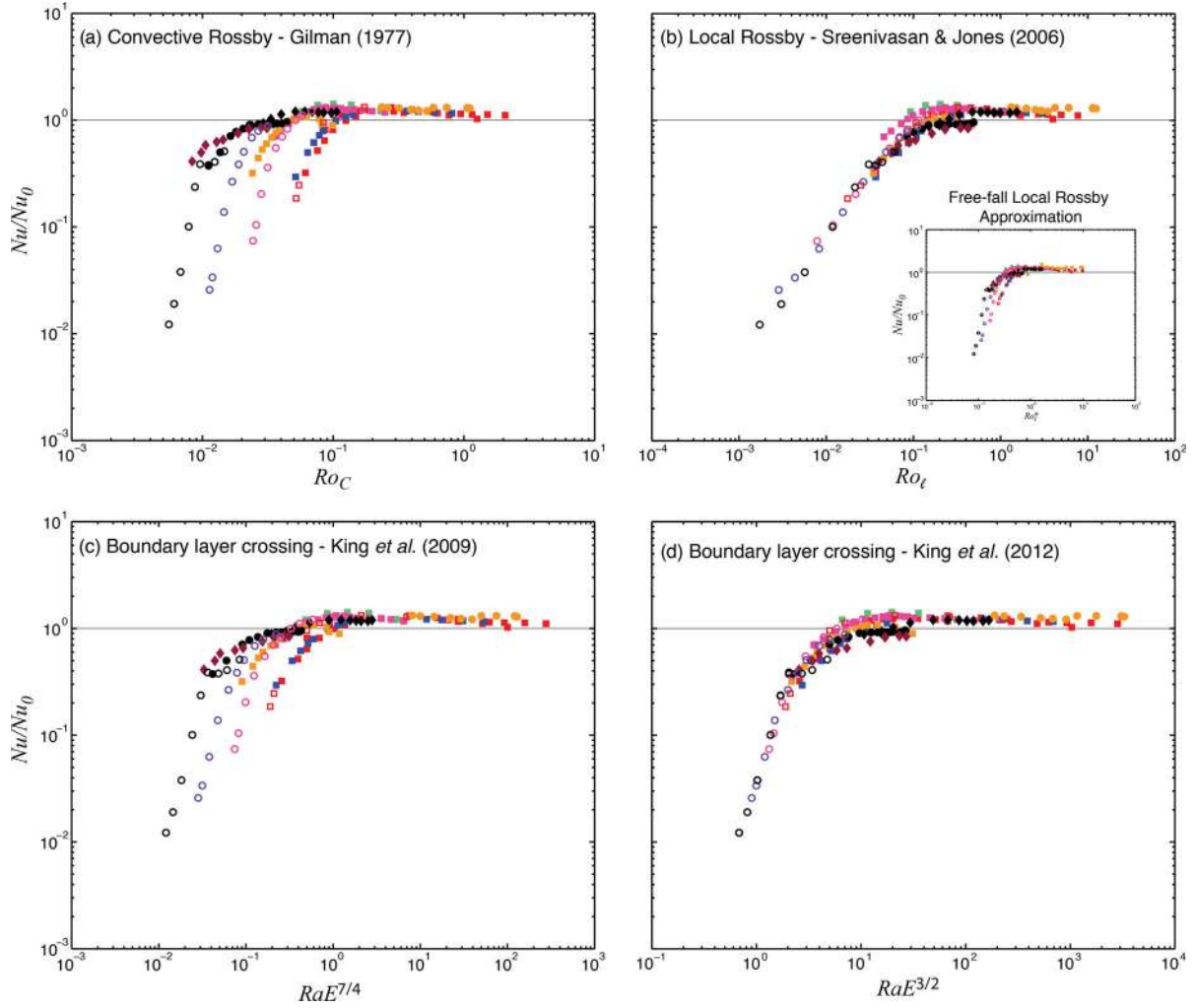


**Figure 8.** Tests of various heat transfer transition arguments. Data are from laboratory ( $Pr \simeq 7$ ) and numerical ( $Pr = 7$ ) rotating convection experiments with  $E \leq 10^{-4}$ . Symbols are as defined in Fig. 5. The non-dimensional heat transfer, normalized by the weakly rotating trend  $Nu_0 = 0.16Ra^{0.284}$ , is plotted against several proposed transition parameters. (a) Conective Rossby transition,  $Ro_C = (RaE^2/Pr)^{1/2}$ . (b) Local Rossby transition (e.g. Sreenivasan & Jones 2006b) estimated using heat transfer parameters,  $\widetilde{Ro}_\ell = c_3^{-1} \widetilde{Re} E^{2/3}$  based upon the velocity scaling from King *et al.* (2013) (see text for details). The inset figure tests a different estimate for local Rossby,  $Ro_\ell^* = (\gamma g \Delta T)/(\Omega L^{1/2})$ , where the free-fall velocity scaling is assumed. (c) Boundary layer crossing transition proposed by King *et al.* (2009),  $RaE^{7/4}$ . (d) Boundary layer crossing transition proposed by King *et al.* (2012),  $RaE^{3/2}$ .

Earth's core,  $E = 10^{-15}$ . Here, we do not consider magnetic field effects, geometrical effects and differences in fluid  $Pr$  values. We also extrapolate our best-fitting RBC scaling law,  $Nu = 0.075Ra^{0.322}$ , to represent an upper bound for the rapidly rotating regime at planetary conditions. Another RBC scaling that may apply at such extreme  $Nu$ – $Ra$  values is the  $Nu = c_4Ra^{1/2}$  law (Kraichnan 1962), where  $c_4$  is an undetermined pre-factor. Here we suppose that the  $1/2$  law branches off from the  $1/3$  law at  $Ra \gtrsim 10^{17}$  (cf. Niemela *et al.* 2000), giving  $c_4 = 1.1 \times 10^{-4}$ . From (18), columnar convection is estimated to be stable for  $Ra_{T_1} \lesssim 60Ra_C$  using the  $\alpha = 1/3$  RBC law and  $Ra_{T_2} \lesssim 150Ra_C$  using the  $\alpha = 1/2$  RBC law.

Fig. 10 shows both of these transition estimates in the context of  $Nu$ – $Ra$  approximations for the Earth's core. The values of  $Ra_T/Ra_C$  presented here may represent an upper bound on the extent of the columnar regime. First, the slope of the rapidly rotating regime continues to steepen with decreasing Ekman number for our available data (Fig. 6). If this trend continues, then the columnar regime is stable for an even smaller region than indicated on Fig. 10. Secondly, the  $E \rightarrow 0$  models of Julien *et al.* (2012a,b) show that columnar convection can break down into geostrophic turbulence well before the

intersection of the steep scaling trend with the RBC trend, further implying a limited range of stability for columns.

Although experimental studies utilize  $Ra$  and  $Nu$  to characterize rotating convection systems, these quantities are nearly impossible to accurately determine in Earth's core. Typical estimates of the core Rayleigh number range between  $10^{20} \lesssim Ra \lesssim 10^{30}$  (e.g. Gubbins 2001; Kono & Roberts 2002; Aurnou *et al.* 2003; Schubert & Soderlund 2011; Roberts & King 2013). However, some estimates are as low as  $10^{15}$  (Roberts & Aurnou 2012) while others are as high as  $10^{38}$  (Gubbins 2001). The (superadiabatic) Nusselt number in the core is also very poorly constrained. In contrast, the flux Rayleigh number,

$$Ra_F = Ra Nu = \frac{\gamma g L^4 q_{sa}}{k \kappa \nu}, \quad (25)$$

can be directly estimated in Earth's core, because it depends only on physical and chemical properties and the superadiabatic heat flux from the core,  $q_{sa}$ . These values can, in turn, be estimated based on observable quantities. A broad range of upper and lower bound estimates for each of these quantities are given in Table 3.

The associated range of  $Ra_F$  is far more tightly constrained than estimates of  $Ra$  in Earth's core:  $6 \times 10^{27} \lesssim Ra_F \lesssim 3 \times 10^{32}$ . This  $Ra_F$  range is shown as the diagonal grey stripe on the figure's right-hand side in Fig. 10. Using only the recent thermal conductivity estimate from Pozzo *et al.* (2012) would yield a slightly lower upper bounding value for  $Ra_F$  of  $2 \times 10^{31}$ . The dashed line connecting  $Ra_C \simeq 10^{21}$  to  $Ra_{T_1} \simeq 6 \times 10^{22}$  and  $Ra_{T_2} \simeq 1.5 \times 10^{23}$  is the extrapolation of our laboratory-numerical findings to Earth's core parameters. We find that our heat transfer extrapolations predominantly intersect core  $Ra_F$  estimates such that  $Ra \gtrsim Ra_T$ , suggesting that rotating convective flows in the core will not be columnar and are instead likely to be comprised of more complex motions.

## 7 DISCUSSION

The results of our suite of laboratory-numerical Rayleigh-Bénard and rotating convection experiments show the overarching behaviours of Boussinesq convection in right cylindrical tanks (laboratory) and in doubly periodic Cartesian domains (numerical).

We find that RBC physics is essential to our understanding of rotating convection systems. At low Ekman numbers, as are relevant to planets and stars, the RBC trend provides the upper bound for heat transfer in our rotating convection experiments. In addition, at high  $Ra$ , our results show that the RBC heat transfer follows predictions from turbulent convection theory (e.g. Malkus 1954; Ahlers *et al.* 2009) providing an important tie between RBC and the

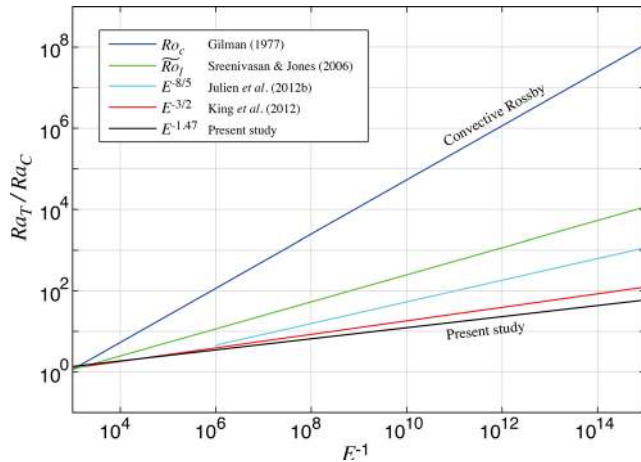


**Figure 9.** Estimated values of  $Ra_T/Ra_C$  for  $E$  ranging from  $10^{-3}$  to  $10^{-15}$ . These values approximate the range,  $Ra_C < Ra < Ra_T$ , over which different models predict the existence of axially coherent convection columns. For  $E \gtrsim 10^{-6}$ , the King *et al.* (2012) transition of  $Ra_T \sim E^{-3/2}$  is nearly indistinguishable from the present fit of  $Ra_T \sim E^{-1.47}$ . The light blue curve is terminated above  $E = 10^{-6}$  because Julien *et al.*'s (2012b) asymptotic model is valid in the limit of low  $E$ . In calculating the  $Ro_c \sim 1$  and  $Ro_l \sim 1$  curves, we assume  $Pr = 10^{-1}$  (Table 3).

**Table 2.** Estimates under Earth-like conditions ( $E = 10^{-15}$ ;  $Pr = 10^{-1}$ ) for the transition Rayleigh number ( $Ra_T$ ) at which columns become unstable as well as the predicted range of column stability ( $Ra_T/Ra_C$ ).

Transition argument	Reference	$Ra_T$	$Ra_T/Ra_C$
$Ro_c \sim 1$	Gilman (1977)	$\sim 10^{29}$	$\sim 10^8$
$Ro_l \sim 1$	Sreenivasan & Jones (2006b)	$\sim 10^{25}$	$\sim 10^4$
$RaE^{8/5} \sim 1$	Julien <i>et al.</i> (2012b)	$\sim 10^{24}$	$\simeq 1100$
$RaE^{3/2} \sim 1$	King <i>et al.</i> (2012)	$\sim 10^{23}$	$\simeq 120$
$RaE^{1.47} \sim 1$	This study	$\sim 10^{23}$	$\simeq 60$

behavioural regimes of rotating convection and convection-driven dynamo systems.

Our experiments show that rotating convection columns carry heat with great efficiency. In particular, our  $Pr \simeq 7$ ,  $E \simeq 10^{-7}$  data provides a heat transfer scaling exponent of  $\beta \simeq 3.6$ , which exceeds even the cubic predictions of King *et al.* (2012). Furthermore, Fig. 6 yields an ever-steepening  $\beta$  value as Ekman is decreased, suggesting that the convection physics of rapidly rotating systems has not yet been fully described. An open question remains whether, and to what extent, the scaling exponent in the steep scaling regime will continue to steepen with decreasing  $E$  (cf. Stellmach *et al.* 2014; Grooms & Whitehead 2015).

The question also remains how the change in heat transfer scalings and the breakdown in coherent columns are mechanistically connected. For instance, do boundary layer nesting phenomena break the columns or vice versa? Further, does the steep heat transfer scaling break down due to the boundary layer physics (e.g. King *et al.* 2012) or due to changes in the interior flow patterns (e.g. Julien *et al.* 2012b)?

Our present study only considers the hydrodynamic behaviour of core-style convection. Theoretical studies predict that the presence of magnetic fields will destabilize columnar convective flows (Chandrasekhar 1961; Eltayeb & Roberts 1970; Roberts & King 2013). In that case, our present hydrodynamic results may provide an upper bound on the stability range of local-scale columns. However, it still remains to be directly determined how strong magnetic fields affect the heat transfer and stability of high  $Ra$  flows in low  $E$ , low  $Pr$  core settings (cf. Aurnou & Olson 2001; Jones *et al.* 2003; Gillet *et al.* 2007).

In spherical shell geometries, low latitude convection columns (outside the tangent cylinder) substantively differ from columnar flows at high latitudes (as simulated in our cylindrical and Cartesian experiments) (e.g. Busse & Cuong 1977; cf. Calkins *et al.* 2013). While specific heat transfer scalings will likely differ at lower latitudes, we predict the same fundamental physical behaviours as found here: a regime of steep convective heat transfer affiliated with the existence of coherent, axial columns that merges with the RBC heat transfer trend at high  $Ra$ , where rotating fluid motions lose their axial coherency. The specific differences between high and low latitude rotating convection behaviours provide an open topic for future research.

Our combination of laboratory-numerical and theoretical models affords a novel view of rapidly rotating (non-magnetic) convection as planetary conditions are approached. As the Ekman number is decreased through larger-scale laboratory experiments and better-resolved computations, the parameter space in which coherent convection columns exist is found to dwindle. Because columns exist only in a limited range of  $Ra$  before they break down, coherent columns as found in present-day models may not be stable at core conditions. We hypothesize, then, that large-scale flow structures in planetary cores, such as system-scale columns, are not a *direct* result of rotating convection. Instead, we hypothesize that convection occurs in the form of 3-D geostrophic turbulence on smaller scales, whose energy then cascades upwards to larger-scale quasi-2-D flows (e.g. Mininni & Pouquet, 2010; Käpylä *et al.* 2011; Chan & Mayr 2013; Favier *et al.* 2014; Guervilly *et al.* 2014; Rubio *et al.* 2014; Stellmach *et al.* 2014; Nataf & Schaeffer 2015), which are capable of efficiently generating observable magnetic fields. Ultimately, our findings suggest the need to revise current planetary dynamo models to include the effects of multiscale rotating convection dynamics and to determine how such flows produce planetary dynamo action.

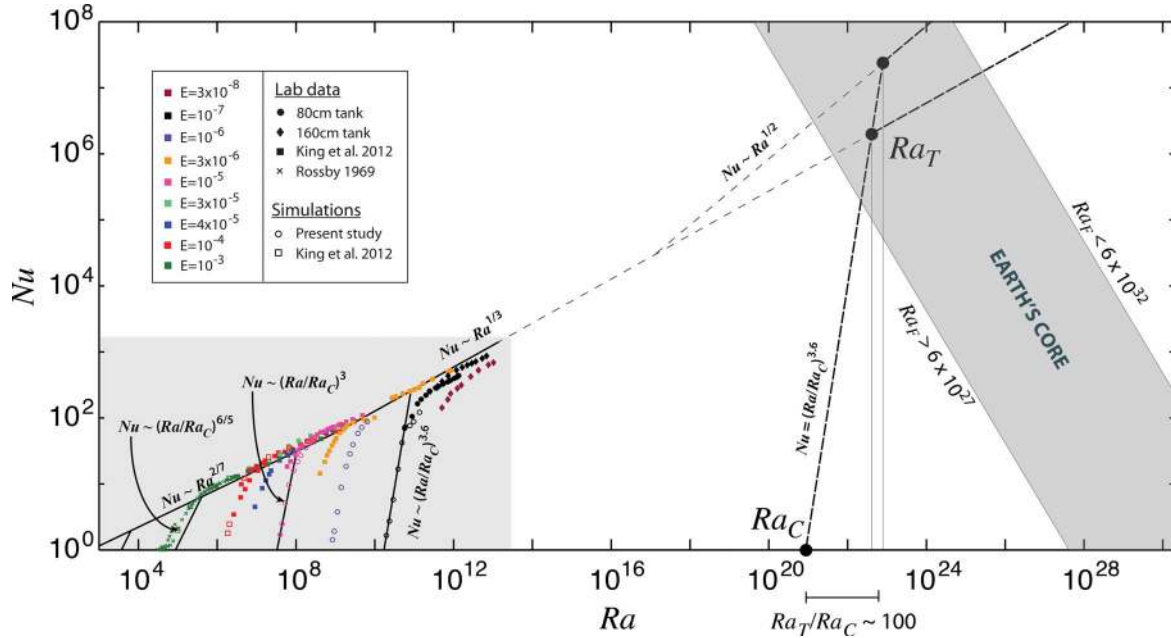


**Figure 10.** Comparison between laboratory-numerical heat transfer data (predominantly at  $Pr \simeq 7$ ) and estimated ranges of heat transfer parameters in Earth's core ( $Pr \simeq 10^{-1}$  to  $10^{-2}$ ). In the lower left hand corner of this figure, we plot all our  $Nu$ - $Ra$  data as well as the best-fitting trends discussed in Figs 4 and 5. Here, we show the  $Nu \sim Ra^{1/3}$  and  $Nu \sim Ra^{1/2}$  scalings for  $Ra \gtrsim 10^{13}$  since centrifugal effects are not relevant in the core. The range of accessible  $Nu$ - $Ra$  space for convection in Earth's core is denoted by the diagonal grey stripe on the figure's right side. The bounds on this diagonal stripe are defined by the maximum and minimum possible values of the superadiabatic flux Rayleigh number in Earth's core,  $6 \times 10^{27} \lesssim Ra_F \lesssim 3 \times 10^{32}$  (see text for details). Extrapolating our lowest available Ekman number results to core conditions, we find that our heat transfer scalings (thick dashed lines) intersect core  $Nu$ - $Ra$  estimates predominantly in the vicinity of and beyond the transition Rayleigh number,  $Ra_T$ . Since columnar convection breaks down near  $Ra_T$ , we hypothesize that local-scale columnar convection structures are not likely to exist in Earth's core.

**Table 3.** Core property estimates used in calculating the bounding flux Rayleigh number values shown in Fig. 10.

Symbol	Parameter	Lower bound	Upper bound	Sources (lower bound; upper bound)
$\gamma$	Thermal expansivity [ $K^{-1}$ ]	$10^{-5}$	$1.8 \times 10^{-5}$	Buffett (2000); Stacey (2007)
$g$	Gravitational acceleration [ $ms^{-2}$ ]	5	11	$g$ at ICB; $g$ at CMB (Dziewonski & Anderson 1981)
$L$	Layer thickness [m]	$2.3 \times 10^6$	$3.5 \times 10^6$	Thickness of outer core; diameter of outer core (Dziewonski & Anderson 1981)
$\nu$	Viscosity [ $m^2s^{-1}$ ]	$10^{-7}$	$10^{-6}$	Buffett (2000); Roberts & King (2013)
$k$	Thermal conductivity [ $W m^{-1} K^{-1}$ ]	30	100	Stacey & Davis (2008); Pozzo <i>et al.</i> (2012)
$\rho$	Density [ $kg m^{-3}$ ]	$9 \times 10^3$	$1.2 \times 10^4$	$\rho$ at CMB; $\rho$ at ICB (Stacey 2007)
$C_p$	Specific heat [ $JK^{-1}kg^{-1}$ ]	790	815	$C_p$ at CMB; $C_p$ at ICB (Stacey 2007)
$\kappa$	Thermal diffusivity [ $m^2s^{-1}$ ]	$3 \times 10^{-6}$	$10^{-5}$	Estimated using above values of $k$ , $\rho$ and $C_p$
$q_{sa}$	Superadiabatic heat flux [ $W m^{-2}$ ]	$6.5 \times 10^{-3}$	$6.5 \times 10^{-2}$	1–10 TW of total heating power (Buffett 2003)

## ACKNOWLEDGEMENTS

The authors wish to thank Nathanaël Schaeffer and an anonymous referee for constructive reviews that greatly improved this manuscript. The authors also thank Michael Calkins, Keith Julien and Krista Soderlund for fruitful scientific discussions. JSC, AR, AG and JMA gratefully acknowledge the financial support of the NSF Geophysics Program. EMK acknowledges the support of the Miller Institute for Basic Research in Science. SS carried out numerical simulations via the support of the John von Neuman Institute for Computing in Jülich, Germany.

## REFERENCES

Ahlers, G. & Xu, X., 2001. Prandtl-number dependence of heat transport in turbulent Rayleigh-Bénard convection, *Phys. Rev. Lett.*, **86**, 3320, doi:10.1103/PhysRevLett.86.3320.  
 Ahlers, G., Grossmann, S. & Lohse, D., 2009. Heat transfer and large scale dynamics in turbulent Rayleigh-Bénard convection, *Rev. Mod. Phys.*, **81**, 503.

Aurnou, J.M., 2007. Planetary core dynamics and convective heat transfer scaling, *Geophys. Astrophys. Fluid Dyn.*, **2**, 327–345.  
 Aurnou, J., Andreadis, S., Zhu, L. & Olson, P., 2003. Experiments on convection in Earth's core tangent cylinder, *Earth planet. Sci. Lett.*, **212**, 119–134.  
 Aurnou, J.M. & Olson, P.L., 2001. Experiments on Rayleigh-Bénard convection, magnetoconvection and rotating magnetoconvection in liquid gallium, *J. Fluid Mech.*, **430**, 283–307.  
 Aurnou, J.M., Heimpel, M. & Wicht, J., 2007. The effects of vigorous mixing in a convective model of zonal flow on the giants, *Icarus*, **190**, 110–126.  
 Braginsky, S.I. & Meytlis, V.P., 1990. Local turbulence in the Earth's core, *Geophys. Astrophys. Fluid Dyn.*, **55**, 71–87.  
 Buffett, B.A., 2000. Dynamics of the Earth's core, *Earth's Deep Interior: Mineral Physics and Tomography From the Atomic to the Global Scale*, pp. 37–62, eds Karato, S. *et al.*, AGU.  
 Buffett, B.A., 2003. The thermal state of Earth's core, *Science*, **299**, 1675–1677.  
 Busse, F.H. & Cuong, P.G., 1977. Convection in rapidly rotating spherical fluid shells, *Geophys. Astrophys. Fluid Dyn.*, **8**, 17–41.

- Calkins, M.A., Julien, K. & Marti, P., 2013. Three-dimensional quasi-geostrophic convection in the rotating cylindrical annulus with steeply sloping end walls, *J. Fluid Mech.*, **732**, 214–244.
- Castaing, B., Gunaratne, G., Kadanoff, L., Libchaber, A. & Heslot, F., 1989. Scaling of hard thermal turbulence in Rayleigh–Bénard convection, *J. Fluid Mech.*, **204**, 1–30.
- Cébron, D., Maubert, P. & Le Bars, M., 2010. Tidal instability in a rotating and differentially heated ellipsoidal shell, *Geophys. J. Int.*, **182**, 1311–1318.
- Chan, K.L. & Mayr, H.G., 2013. Numerical simulation of convectively generated vortices: application to the Jovian planets, *Earth planet. Sci. Lett.*, **371–372**, 212–219.
- Chandrasekhar, S., 1961. *Hydrodynamics and Hydromagnetic Stability*, Oxford Univ. Press.
- Chillá, F., Ciliberto, S., Innocenti, C. & Pampaloni, E., 1993. Boundary layer and scaling properties in turbulent thermal convection, *Il Nuovo Cimento D*, **15**, 1229–1249.
- Christensen, U.R., 2002. Zonal flow driven by strongly supercritical convection in rotating spherical shells, *J. Fluid Mech.*, **470**, 115–133.
- Christensen, U.R., 2010. Dynamo scaling laws and applications to the planets, *Space Sci. Rev.*, **152**, 565–590.
- Christensen, U.R. & Aubert, J., 2006. Scaling properties of convection-driven dynamos in rotating spherical shells and application to planetary magnetic fields, *Geophys. J. Int.*, **166**, 97–114.
- Cioni, S., Chaumat, S. & Sommeria, J., 2000. Effect of a vertical magnetic field on turbulent Rayleigh–Bénard convection, *Phys. Rev. E*, **62**, R4520.
- de Koker, N., Steinle-Neumann, G. & Vlček, V., 2012. Electrical resistivity and thermal conductivity of liquid Fe alloys at high P and T, and heat flux in Earth's core, *Proc. Natl. Acad. Sci. U.S.A.*, **109**, 4070–4073.
- Dziewonski, A.M. & Anderson, D.L., 1981. Preliminary reference Earth model, *Phys. Earth planet. Inter.*, **25**, 297–356.
- Ecke, R. & Niemela, J., 2014. Heat transport in the geostrophic regime of rotating Rayleigh–Bénard convection, *Phys. Rev. Lett.*, **113**, 114301.
- Eltayeb, I.A. & Roberts, P.H., 1970. On the hydromagnetics of rotating fluids, *Astrophys. J.*, **162**, 699–701.
- Favier, B., Silvers, L.J. & Proctor, M.R.E., 2014. Inverse cascade and symmetry breaking in rapidly rotating Boussinesq convection, *Phys. Fluids*, **26**, 096605.
- Funfschilling, D., Brown, E., Nikolaenko, A. & Ahlers, G., 2005. Heat transport by turbulent Rayleigh–Bénard convection in cylindrical samples with aspect ratio one and larger, *J. Fluid Mech.*, **536**, 145–154.
- Gastine, T., Wicht, J. & Aurnou, J.M., 2013. Zonal flow regimes in rotating anelastic spherical shells: an application to giant planets, *Icarus*, **225**, 156–172.
- Gastine, T., Yadav, R.K., Morin, J., Reiners, A. & Wicht, J., 2014. From solar-like to antisolar differential rotation in cool stars, *MNRAS*, **438**, L76–L80.
- Gillet, N., Brito, D., Jault, D. & Nataf, H.C., 2007. Experimental and numerical studies of magnetoconvection in a rapidly rotating spherical shell, *J. Fluid Mech.*, **580**, 123–143.
- Gilman, P.A., 1977. Nonlinear dynamics of Boussinesq convection in a deep rotating shell – I, *Geophys. Astrophys. Fluid Dyn.*, **8**, 93–135.
- Glatzmaier, G.A. & Roberts, P.H., 1996. Rotation and magnetism of Earth's inner core, *Science*, **274**, 1887–1891.
- Glazier, J.A., Segawa, T., Naert, A. & Sano, M., 1999. Evidence against ‘ultrahard’ thermal turbulence at very high Rayleigh numbers, *Nature*, **398**, 307–310.
- Grooms, I. & Whitehead, J.P., 2015. Bounds on heat transport in rapidly rotating Rayleigh–Bénard convection, *Nonlinearity*, **28**, 29–41.
- Grooms, I., Julien, K., Weiss, J.B. & Knobloch, E., 2010. Model of convective Taylor columns in rotating Rayleigh–Bénard convection, *Phys. Rev. Lett.*, **104**, 224501.
- Grossmann, S. & Lohse, D., 2000. Scaling in thermal convection: a unifying theory, *J. Fluid Mech.*, **407**, 27–56.
- Gubbins, D., 2001. The Rayleigh number for convection in the Earth's core, *Phys. Earth planet. Inter.*, **128**, 3–12.
- Guervilly, C., Hughes, D.W. & Jones, C.A., 2014. Large-scale vortices in rapidly rotating Rayleigh–Bénard convection, *J. Fluid Mech.*, **758**, 407–435.
- Hori, K., Wicht, J. & Christensen, U.R., 2010. The effect of thermal boundary conditions on dynamos driven by internal heating, *Phys. Earth planet. Inter.*, **182**, 85–97.
- Jones, C.A., Mussa, A.I. & Worland, S.J., 2003. Magnetoconvection in a rapidly rotating sphere: the weak-field case, *Proc. R. Soc. Lond. A*, **459**, 773–797.
- Julien, K. & Knobloch, E., 1998. Strongly nonlinear convection cells in a rapidly-rotating fluid layer: the tilted f-plane, *J. Fluid Mech.*, **360**, 141–178.
- Julien, K., Legg, S., McWilliams, J. & Werne, J., 1996. Rapidly rotating turbulent Rayleigh–Bénard convection, *J. Fluid Mech.*, **322**, 243–273.
- Julien, K., Rubio, A.M., Grooms, I. & Knobloch, E., 2012a. Statistical and physical balances in low Rossby number Rayleigh–Bénard convection, *Geophys. Astrophys. Fluid Dyn.*, **106**, 392–428.
- Julien, K., Knobloch, E., Rubio, A.M. & Vasil, G.M., 2012b. Heat transport in low-Rossby-number Rayleigh–Bénard convection, *Phys. Rev. Lett.*, **109**, 254503.
- Kageyama, A. & Sato, T., 1995. Computer simulation of a magnetohydrodynamic dynamo. II., *Phys. Plasmas*, **2**, 1421–1431.
- Käpylä, P.J., Mantere, M.J. & Hackman, T., 2011. Starspots due to large-scale vortices in rotating turbulent convection, *Astrophys. J.*, **742**(1), doi:10.1088/0004-637X/742/1/34.
- King, E.M. & Aurnou, J.M., 2012. Thermal evidence for Taylor columns in turbulent rotating Rayleigh–Bénard convection, *Phys. Rev. E*, **85**, 016313.
- King, E.M. & Aurnou, J.M., 2013. Turbulent convection in liquid metal with and without rotation, *Proc. Natl. Acad. Sci. U.S.A.*, **110**, 6688–6693.
- King, E.M. & Aurnou, J.M., 2015. Magnetostrophic turbulence as the optimal state for convective dynamos, *Proc. Natl. Acad. Sci. U.S.A.*, 201417741.
- King, E.M. & Buffett, B.A., 2013. Flow speeds and length scales in geodynamo models: the role of viscosity, *Earth planet. Sci. Lett.*, **371**, 156–162.
- King, E.M., Stellmach, S., Noir, J., Hansen, U. & Aurnou, J.M., 2009. Boundary layer control of rotating convection systems, *Nature*, **457**, 301–304.
- King, E.M., Soderlund, K.M., Christensen, U.R., Wicht, J. & Aurnou, J.M., 2010. Convective heat transfer in planetary dynamo models, *Geochem. Geophys. Geosyst.*, **11**, doi:10.1029/2010GC003053.
- King, E.M., Stellmach, S. & Aurnou, J.M., 2012. Heat transfer by rapidly rotating Rayleigh–Bénard convection, *J. Fluid Mech.*, **691**, 568–582.
- King, E.M., Stellmach, S. & Buffett, B.A., 2013. Scaling behavior in Rayleigh–Bénard convection with and without rotation, *J. Fluid Mech.*, **717**, 449–471.
- Kono, M. & Roberts, P.H., 2002. Recent geodynamo simulations and observations of the geomagnetic field, *Rev. Geophys.*, **40**, 4-1–4-53.
- Kraichnan, R.H., 1962. Turbulent thermal convection at arbitrary Prandtl number, *Phys. Fluids*, **5**, 1374.
- Kunnen, R.P.J., Clercx, H.J.H. & Geurts, B.J., 2008. Breakdown of large-scale circulation in turbulent rotating convection, *Europhys. Lett.*, **84**, 24001, doi:10.1209/0295-5075/84/24001.
- Liu, Y. & Ecke, R.E., 1997. Heat transport scaling in turbulent Rayleigh–Bénard convection: effects of rotation and Prandtl number, *Phys. Rev. Lett.*, **79**, 2257–2260.
- Malkus, W.V.R., 1954. The heat transport and spectrum of thermal turbulence, *Proc. R. Soc. Lond. A*, **225**, 196–212.
- Marques, F., Mercader, I., Batiste, O. & Lopez, J.M., 2007. Centrifugal effects in rotating convection: axisymmetric states and three-dimensional instabilities, *J. Fluid Mech.*, **580**, 303–318.
- Mininni, P.D. & Pouquet, A., 2010. Rotating helical turbulence. I. Global evolution and spectral behavior, *Phys. Fluids*, **22**, 035105.
- Miyagoshi, T., Kageyama, A. & Sato, T., 2010. Zonal flow formation in the Earth's core, *Nature*, **463**, 793–796.
- Nakagawa, Y. & Frenzen, P., 1955. A theoretical and experimental study of cellular convection in rotating fluids, *Tellus*, **7**, 1–21.
- Nataf, H.-C. & Schaeffer, N., 2015. Turbulence in the core, *Treatise on Geophysics*, 2nd edn, Vol. 8: Core Dynamics, eds Olson, P., Schubert, G. & Elveier, B.V., in press.
- Niemela, J.J. & Sreenivasan, K.R., 2006. Turbulent convection at high Rayleigh numbers and aspect ratio 4, *J. Fluid Mech.*, **557**, 411–422.

- Niemela, J.J., Skrbek, L., Sreenivasan, K.R. & Donnelly, R.J., 2000. Turbulent convection at very high Rayleigh numbers, *Nature*, **404**, 837–840.
- Niiler, P.P. & Bisshopp, F.E., 1965. On the influence of Coriolis force on onset of thermal convection, *J. Fluid Mech.*, **22**, 753–761.
- Olson, P.L., Glatzmaier, G.A. & Coe, R.S., 2011. Complex polarity reversals in a geodynamo model, *Earth planet. Sci. Lett.*, **304**, 168–179.
- Pellew, A. & Southwell, R.V., 1940. On maintained convective motion in a fluid heated from below, *Proc. Roy. Soc. Lond. A.*, **176**, 312–343.
- Pozzo, M., Davies, C., Gubbins, D. & Alfè, D., 2012. Thermal and electrical conductivity of iron at Earth's core conditions, *Nature*, **485**, 355–358.
- Ribeiro, A., Guermond, J.-L., Fabre, G. & Aurnou, J.M., 2015. Canonical models of geophysical and astrophysical flows: turbulent convection experiments in liquid metals, *Metals*, in press.
- Roberts, P.H. & Aurnou, J.M., 2012. On the theory of core-mantle coupling, *Geophys. Astrophys. Fluid Dyn.*, **106**, 157–230.
- Roberts, P.H. & King, E.M., 2013. On the genesis of the Earth's magnetism, *Rep. Prog. Phys.*, **76**, 096801.
- Roche, P.E., Gauthier, F., Kaiser, R. & Salort, J., 2010. On the triggering of the Ultimate Regime of convection, *N. J. Phys.*, **12**, 085014.
- Rossby, H.T., 1969. A study of Bénard convection with and without rotation, *J. Fluid Mech.*, **36**, 309–335.
- Rubio, A.M., Julien, K., Knobloch, E. & Weiss, J.B., 2014. Upscale energy transfer in three-dimensional rapidly rotating turbulent convection, *Phys. Rev. Lett.*, **112**, 144501.
- Schmitz, S. & Tilgner, A., 2009. Heat transport in rotating convection without Ekman layers, *Phys. Rev. E.*, **80**, 015305.
- Schubert, G. & Soderlund, K.M., 2011. Planetary magnetic fields: observations and models, *Phys. Earth planet. Inter.*, **187**, 92–108.
- Shraiman, B.I. & Siggia, E.D., 1990. Heat transport in high-Rayleigh-number convection, *Phys. Rev. A.*, **42**, 3650–3653.
- Soderlund, K.M., King, E.M. & Aurnou, J.M., 2012. The influence of magnetic fields in planetary dynamo models, *Earth planet. Sci. Lett.*, **333**, 9–20.
- Soderlund, K.M., Heimpel, M.H., King, E.M. & Aurnou, J.M., 2013. Turbulent models of ice giant internal dynamics: dynamos, heat transfer, and zonal flows, *Icarus*, **224**, 97–113.
- Soderlund, K.M., Schmidt, B.E. & Wicht, J., 2014. Ocean-driven heating of Europa's icy shell at low latitudes, *Nat. Geosci.*, **7**, 16–19.
- Spiegel, E.A., 1971. Convection in stars: I. Basic Boussinesq convection, *Annu. Rev. Astron. Astrophys.*, **9**, 323–352.
- Sprague, M., Julien, K., Knobloch, E. & Werne, J., 2006. Numerical simulation of an asymptotically reduced system for rotationally constrained convection, *J. Fluid Mech.*, **551**, 141–174.
- Sreenivasan, B. & Jones, C.A., 2006a. Azimuthal winds, convection and dynamo action in the polar regions of planetary cores, *Geophys. Astrophys. Fluid Dyn.*, **100**, 319–339.
- Sreenivasan, B. & Jones, C.A., 2006b. The role of inertia in the evolution of spherical dynamos, *Geophys. J. Int.*, **164**, 467–476.
- Stacey, F.D., 2007. *Core Properties, Physical in Encyclopedia of Geomagnetism and Paleomagnetism*, Springer-Verlag, pp. 91–94.
- Stacey, F.D. & Davis, P.M., 2008. *Physics of the Earth*, Cambridge Univ. Press.
- Stellmach, S. & Hansen, U., 2004. Cartesian convection driven dynamos at low Ekman number, *Phys. Rev. E.*, **70**, 056312.
- Stellmach, S. & Hansen, U., 2008. An efficient spectral method for the simulation of dynamos in Cartesian geometry and its implementation on massively parallel computers, *Geochem. Geophys. Geosyst.*, **9**, doi:10.1029/2007GC001778.
- Stellmach, S., Lischper, M., Julien, K., Vasil, G., Cheng, J.S., Ribeiro, A., King, E.M. & Aurnou, J.M., 2014. Approaching the asymptotic regime of rapidly rotating convection: boundary layers vs interior dynamics, *Phys. Rev. Lett.*, **113**, 254501.
- Stevens, R.J., Clercx, H.J. & Lohse, D., 2013. Heat transport and flow structure in rotating Rayleigh-Bénard convection, *Eur. J. Mech.*, **40**, 41–49.
- Takehiro, S.I., 2008. Physical interpretation of spiralling-columnar convection in a rapidly rotating annulus with radial propagation properties of Rossby waves, *J. Fluid Mech.*, **614**, 67–86.
- Wu, X.Z. & Libchaber, A., 1992. Scaling relations in thermal turbulence: the aspect-ratio dependence, *Phys. Rev. A.*, **45**, 842–845.
- Zhang, K. & Schubert, G., 2000. Magnetohydrodynamics in rapidly rotating spherical systems, *Annu. Rev. Fluid Mech.*, **32**, 409–443.
- Zhong, J.Q. & Ahlers, G., 2010. Heat transport and the large-scale circulation in rotating turbulent Rayleigh-Bénard convection, *J. Fluid Mech.*, **665**, 300–333.

## APPENDIX

**Table A1.** Laboratory convection data. Here,  $\bar{\tau}$  denotes the averaging time in thermal diffusion time scale units  $L^2/\kappa$ . Note that  $\tau \ll 1$  in all our experiments. However, the time series data have reached a statistical steady state prior to the start of data acquisition in all the cases. Before acquisition, each case is allowed to equilibrate for approximately 12 hr until the variation in mean temperature is less than 1 per cent. Data is then acquired for at least 2 hr per case (see Section 3.1).

Height (m)	rpm	Power (W)	Mean $T$ (°C)	$\Delta T$ (°C)	$Pr$	$E$	$Ra$	$Nu$	$\bar{\tau}$
0.798	0	9.58	23.31	2.88	6.338	$\infty$	$2.626 \times 10^{10}$	166.85	$2.25 \times 10^{-3}$
0.798	0	9.83	23.12	2.60	6.370	$\infty$	$2.341 \times 10^{10}$	166.89	$1.31 \times 10^{-3}$
0.798	0	14.87	23.52	3.82	6.301	$\infty$	$3.529 \times 10^{10}$	176.49	$2.29 \times 10^{-3}$
0.798	0	19.72	24.39	4.56	6.159	$\infty$	$4.430 \times 10^{10}$	193.42	$8.72 \times 10^{-4}$
0.798	0	30.05	23.14	6.49	6.365	$\infty$	$5.851 \times 10^{10}$	210.89	$1.44 \times 10^{-3}$
0.798	0	39.18	22.81	7.76	6.422	$\infty$	$6.847 \times 10^{10}$	230.07	$1.51 \times 10^{-3}$
0.798	0	49.42	22.87	9.32	6.412	$\infty$	$8.260 \times 10^{10}$	242.17	$1.66 \times 10^{-3}$
0.798	0	69.10	23.60	11.75	6.288	$\infty$	$1.090 \times 10^{11}$	264.23	$1.70 \times 10^{-3}$
0.798	0	98.52	24.57	14.90	6.129	$\infty$	$1.464 \times 10^{11}$	294.33	$2.07 \times 10^{-3}$
0.798	0	149.26	23.15	21.17	6.365	$\infty$	$1.908 \times 10^{11}$	316.30	$1.04 \times 10^{-3}$
0.798	0	197.37	26.12	24.60	5.889	$\infty$	$2.639 \times 10^{11}$	353.37	$1.54 \times 10^{-3}$
0.798	0	244.96	26.30	29.11	5.861	$\infty$	$3.155 \times 10^{11}$	374.03	$1.71 \times 10^{-3}$
0.798	0	294.56	28.60	31.94	5.531	$\infty$	$3.905 \times 10^{11}$	401.58	$1.20 \times 10^{-3}$
0.798	0	341.22	31.01	35.02	5.214	$\infty$	$4.807 \times 10^{11}$	424.39	$1.64 \times 10^{-3}$
0.798	0	394.31	33.40	37.72	4.926	$\infty$	$5.757 \times 10^{11}$	448.27	$1.17 \times 10^{-3}$
0.798	0	495.68	39.41	41.57	4.299	$\infty$	$8.047 \times 10^{11}$	503.15	$1.77 \times 10^{-3}$
0.798	0	495.56	39.42	41.58	4.298	$\infty$	$8.053 \times 10^{11}$	503.19	$1.61 \times 10^{-3}$
0.798	0	543.07	41.51	43.61	4.108	$\infty$	$9.100 \times 10^{11}$	520.14	$1.87 \times 10^{-3}$
0.798	2	14.70	23.47	3.24	6.311	$3.43 \times 10^{-6}$	$2.976 \times 10^{10}$	200.34	$1.91 \times 10^{-3}$

**Table A1** (Continued.)

Height (m)	rpm	Power (W)	Mean $T$ ( $^{\circ}\text{C}$ )	$\Delta T$ ( $^{\circ}\text{C}$ )	$Pr$	$E$	$Ra$	$Nu$	$\bar{\tau}$
0.798	2	19.76	23.92	3.95	6.235	$3.39 \times 10^{-6}$	$3.739 \times 10^{10}$	210.25	$1.74 \times 10^{-3}$
0.798	2	29.41	25.01	5.58	6.060	$3.31 \times 10^{-6}$	$5.628 \times 10^{10}$	233.18	$1.58 \times 10^{-3}$
0.798	2	49.60	24.13	8.78	6.201	$3.37 \times 10^{-6}$	$8.405 \times 10^{10}$	253.79	$1.52 \times 10^{-3}$
0.798	2	68.94	24.01	11.52	6.221	$3.38 \times 10^{-6}$	$1.095 \times 10^{11}$	269.80	$1.43 \times 10^{-3}$
0.798	2	99.61	23.81	15.54	6.254	$3.40 \times 10^{-6}$	$1.459 \times 10^{11}$	287.72	$1.74 \times 10^{-3}$
0.798	2	149.13	23.34	20.07	6.332	$3.44 \times 10^{-6}$	$1.831 \times 10^{11}$	331.53	$1.41 \times 10^{-3}$
0.798	2	248.44	26.96	28.07	5.764	$3.16 \times 10^{-6}$	$3.152 \times 10^{11}$	386.23	$1.89 \times 10^{-3}$
0.798	2	493.03	39.39	41.63	4.301	$2.44 \times 10^{-6}$	$8.053 \times 10^{11}$	499.11	$1.88 \times 10^{-3}$
0.798	2	543.30	41.59	43.86	4.101	$2.34 \times 10^{-6}$	$9.178 \times 10^{11}$	516.85	$1.90 \times 10^{-3}$
0.798	2	495.68	39.41	41.57	4.299	$2.44 \times 10^{-6}$	$8.047 \times 10^{11}$	503.15	$1.87 \times 10^{-3}$
0.798	60	9.80	24.95	6.19	6.069	$1.10 \times 10^{-7}$	$6.215 \times 10^{10}$	69.62	$1.41 \times 10^{-3}$
0.798	60	20.09	26.77	8.66	5.792	$1.06 \times 10^{-7}$	$9.629 \times 10^{10}$	105.48	$1.92 \times 10^{-3}$
0.798	60	49.76	24.16	13.79	6.197	$1.12 \times 10^{-7}$	$1.322 \times 10^{11}$	163.69	$1.30 \times 10^{-3}$
0.798	60	69.74	24.78	16.41	6.096	$1.11 \times 10^{-7}$	$1.633 \times 10^{11}$	190.77	$1.93 \times 10^{-3}$
0.798	60	98.31	26.25	19.95	5.868	$1.07 \times 10^{-7}$	$2.157 \times 10^{11}$	220.40	$1.93 \times 10^{-3}$
0.798	60	147.93	25.27	26.04	6.018	$1.10 \times 10^{-7}$	$2.666 \times 10^{11}$	254.53	$1.79 \times 10^{-3}$
0.798	60	201.56	28.36	31.47	5.565	$1.02 \times 10^{-7}$	$3.801 \times 10^{11}$	284.21	$1.79 \times 10^{-3}$
0.798	60	244.13	29.41	35.80	5.421	$9.99 \times 10^{-8}$	$4.556 \times 10^{11}$	301.29	$1.79 \times 10^{-3}$
0.798	60	297.83	32.56	39.86	5.024	$9.34 \times 10^{-8}$	$5.868 \times 10^{11}$	325.33	$1.80 \times 10^{-3}$
0.798	60	491.88	42.77	52.19	4.000	$7.64 \times 10^{-8}$	$1.137 \times 10^{12}$	395.55	$1.80 \times 10^{-3}$
0.798	60	347.30	38.06	41.70	4.429	$8.36 \times 10^{-8}$	$7.677 \times 10^{11}$	350.05	$1.80 \times 10^{-3}$
0.798	60	394.65	40.79	44.51	4.172	$7.93 \times 10^{-8}$	$9.056 \times 10^{11}$	369.48	$1.79 \times 10^{-3}$
0.798	60	544.15	46.43	53.95	3.708	$7.14 \times 10^{-8}$	$1.326 \times 10^{12}$	416.00	$1.77 \times 10^{-3}$
0.798	60	544.12	46.47	54.07	3.705	$7.13 \times 10^{-8}$	$1.330 \times 10^{12}$	414.93	$1.58 \times 10^{-3}$
0.798	60	597.12	48.42	55.80	3.563	$6.89 \times 10^{-8}$	$1.459 \times 10^{12}$	438.69	$1.61 \times 10^{-3}$
0.798	60	597.11	48.52	56.16	3.556	$6.88 \times 10^{-8}$	$1.473 \times 10^{12}$	435.82	$1.63 \times 10^{-3}$
1.595	0	29.56	24.71	5.92	6.107	$\infty$	$4.689 \times 10^{11}$	406.83	$4.54 \times 10^{-4}$
1.595	0	49.74	23.88	9.18	6.241	$\infty$	$6.913 \times 10^{11}$	466.58	$3.20 \times 10^{-4}$
1.595	0	70.12	23.80	11.91	6.255	$\infty$	$8.930 \times 10^{11}$	544.63	$4.52 \times 10^{-4}$
1.595	0	98.01	23.56	15.68	6.295	$\infty$	$1.158 \times 10^{12}$	598.38	$4.52 \times 10^{-4}$
1.595	0	98.12	23.53	15.68	6.301	$\infty$	$1.155 \times 10^{12}$	597.24	$4.51 \times 10^{-4}$
1.595	0	149.08	23.66	21.25	6.278	$\infty$	$1.579 \times 10^{12}$	654.58	$4.52 \times 10^{-4}$
1.595	0	149.18	23.66	21.31	6.279	$\infty$	$1.583 \times 10^{12}$	647.18	$4.51 \times 10^{-4}$
1.595	0	198.79	24.53	26.16	6.136	$\infty$	$2.048 \times 10^{12}$	693.79	$4.54 \times 10^{-4}$
1.595	0	198.82	24.37	26.36	6.163	$\infty$	$2.044 \times 10^{12}$	689.03	$4.52 \times 10^{-4}$
1.595	0	248.39	27.33	29.61	5.710	$\infty$	$2.708 \times 10^{12}$	753.64	$4.57 \times 10^{-4}$
1.595	0	247.77	27.24	29.54	5.723	$\infty$	$2.689 \times 10^{12}$	747.77	$4.55 \times 10^{-4}$
1.595	0	299.24	30.14	32.77	5.326	$\infty$	$3.448 \times 10^{12}$	794.43	$4.61 \times 10^{-4}$
1.595	0	299.26	29.97	32.91	5.347	$\infty$	$3.435 \times 10^{12}$	790.69	$4.60 \times 10^{-4}$
1.595	0	299.30	29.91	32.91	5.355	$\infty$	$3.425 \times 10^{12}$	790.40	$4.59 \times 10^{-4}$
1.595	0	346.29	32.48	35.27	5.034	$\infty$	$4.130 \times 10^{12}$	848.01	$4.65 \times 10^{-4}$
1.595	0	346.28	32.47	35.23	5.035	$\infty$	$4.125 \times 10^{12}$	847.02	$4.64 \times 10^{-4}$
1.595	0	397.08	35.17	38.35	4.727	$\infty$	$5.033 \times 10^{12}$	884.01	$4.69 \times 10^{-4}$
1.595	0	396.82	35.17	38.28	4.728	$\infty$	$5.023 \times 10^{12}$	885.88	$4.26 \times 10^{-4}$
1.595	0	495.21	39.79	43.07	4.264	$\infty$	$6.749 \times 10^{12}$	969.87	$4.73 \times 10^{-4}$
1.595	0	495.15	39.87	43.20	4.256	$\infty$	$6.789 \times 10^{12}$	965.78	$3.83 \times 10^{-4}$
1.595	15	9.98	23.27	3.79	6.344	$1.15 \times 10^{-7}$	$2.750 \times 10^{11}$	250.91	$2.92 \times 10^{-4}$
1.595	15	19.61	24.30	5.46	6.174	$1.12 \times 10^{-7}$	$4.215 \times 10^{11}$	298.44	$4.53 \times 10^{-4}$
1.595	15	19.62	24.28	5.43	6.177	$1.12 \times 10^{-7}$	$4.188 \times 10^{11}$	288.29	$4.54 \times 10^{-4}$
1.595	15	19.62	24.23	5.34	6.185	$1.12 \times 10^{-7}$	$4.107 \times 10^{11}$	290.43	$4.53 \times 10^{-4}$
1.595	15	19.64	24.25	5.37	6.182	$1.12 \times 10^{-7}$	$4.134 \times 10^{11}$	289.31	$1.67 \times 10^{-4}$
1.595	15	29.87	25.20	6.86	6.031	$1.10 \times 10^{-7}$	$5.578 \times 10^{11}$	355.63	$4.55 \times 10^{-4}$
1.595	15	50.04	24.39	10.15	6.159	$1.12 \times 10^{-7}$	$7.879 \times 10^{11}$	433.43	$4.51 \times 10^{-4}$
1.595	15	98.90	24.04	16.96	6.216	$1.13 \times 10^{-7}$	$1.290 \times 10^{12}$	529.05	$4.51 \times 10^{-4}$
1.595	15	150.02	24.46	23.17	6.148	$1.12 \times 10^{-7}$	$1.806 \times 10^{12}$	581.76	$4.54 \times 10^{-4}$
1.595	15	199.44	25.78	28.82	5.940	$1.08 \times 10^{-7}$	$2.424 \times 10^{12}$	628.86	$4.55 \times 10^{-4}$
1.595	15	249.44	28.55	32.39	5.538	$1.02 \times 10^{-7}$	$3.154 \times 10^{12}$	669.95	$4.59 \times 10^{-4}$
1.595	15	249.22	28.59	32.41	5.533	$1.02 \times 10^{-7}$	$3.162 \times 10^{12}$	671.16	$4.57 \times 10^{-4}$
1.595	15	296.54	31.46	35.83	5.157	$9.57 \times 10^{-8}$	$4.009 \times 10^{12}$	713.01	$4.63 \times 10^{-4}$
1.595	15	393.91	36.72	41.65	4.564	$8.59 \times 10^{-8}$	$5.816 \times 10^{12}$	792.88	$4.68 \times 10^{-4}$
1.595	15	481.66	40.87	45.97	4.165	$7.93 \times 10^{-8}$	$7.489 \times 10^{12}$	868.14	$4.73 \times 10^{-4}$
1.595	60	9.88	24.89	6.94	6.079	$2.77 \times 10^{-8}$	$5.545 \times 10^{11}$	142.27	$4.56 \times 10^{-4}$
1.595	60	20.54	26.13	9.09	5.888	$2.69 \times 10^{-8}$	$7.792 \times 10^{11}$	189.83	$2.37 \times 10^{-4}$

**Table A1** (Continued.)

Height (m)	rpm	Power (W)	Mean $T$ (°C)	$\Delta T$ (°C)	$Pr$	$E$	$Ra$	$Nu$	$\bar{\tau}$
1.595	60	29.55	26.82	10.33	5.784	$2.65 \times 10^{-8}$	$9.201 \times 10^{11}$	233.33	$4.41 \times 10^{-4}$
1.595	60	49.54	26.87	15.27	5.777	$2.65 \times 10^{-8}$	$1.362 \times 10^{12}$	279.36	$1.66 \times 10^{-4}$
1.595	60	68.79	27.18	18.93	5.732	$2.63 \times 10^{-8}$	$1.717 \times 10^{12}$	312.75	$2.27 \times 10^{-4}$
1.595	60	148.93	28.27	31.03	5.577	$2.56 \times 10^{-8}$	$2.979 \times 10^{12}$	421.33	$1.92 \times 10^{-4}$
1.595	60	248.21	32.28	40.44	5.058	$2.35 \times 10^{-8}$	$4.695 \times 10^{12}$	526.35	$2.32 \times 10^{-4}$
1.595	60	247.53	32.32	40.44	5.053	$2.35 \times 10^{-8}$	$4.703 \times 10^{12}$	523.84	$2.32 \times 10^{-4}$
1.595	60	395.75	41.11	51.11	4.143	$1.97 \times 10^{-8}$	$8.398 \times 10^{12}$	636.53	$2.38 \times 10^{-4}$
1.595	60	488.78	46.37	57.66	3.713	$1.79 \times 10^{-8}$	$1.129 \times 10^{13}$	686.70	$2.41 \times 10^{-4}$

**Table A2.** Numerical rotating convection data. Here,  $\bar{\tau}$  denotes the time over which the diagnostics have been averaged in thermal diffusion time scale units  $L^2/\kappa$ . Even though millions of time steps were performed,  $\tau < 1$  in all our simulations, such that the quoted temporal averages may not be fully accurate (see e.g. Julien *et al.* 2012a for a discussion of the broad range of timescales involved in rapidly rotating convection). In general however, the averaging times are comparable to or even exceed those used in the laboratory experiments (Table A1).

$Pr$	$E$	$Ra$	$Nu$	$\bar{\tau}$
7	$1.00 \times 10^{-5}$	$4.18 \times 10^7$	1.73	1.05
7	$1.00 \times 10^{-5}$	$4.64 \times 10^7$	2.51	$5.31 \times 10^{-1}$
7	$1.00 \times 10^{-5}$	$5.57 \times 10^7$	5.17	$3.42 \times 10^{-1}$
7	$1.00 \times 10^{-5}$	$6.96 \times 10^7$	9.75	$1.85 \times 10^{-1}$
7	$1.00 \times 10^{-5}$	$9.28 \times 10^7$	16.1	$1.06 \times 10^{-1}$
7	$1.00 \times 10^{-5}$	$1.16 \times 10^8$	21.9	$7.69 \times 10^{-2}$
7	$1.00 \times 10^{-5}$	$1.39 \times 10^8$	27.1	$6.17 \times 10^{-2}$
7	$1.00 \times 10^{-5}$	$1.86 \times 10^8$	35.7	$4.56 \times 10^{-2}$
7	$1.00 \times 10^{-5}$	$2.32 \times 10^8$	42.2	$3.66 \times 10^{-2}$
7	$1.00 \times 10^{-5}$	$3.25 \times 10^8$	50.7	$2.82 \times 10^{-2}$
7	$1.00 \times 10^{-6}$	$9.00 \times 10^8$	1.44	$1.79 \times 10^{-1}$
7	$1.00 \times 10^{-6}$	$1.00 \times 10^9$	1.94	$4.30 \times 10^{-1}$
7	$1.00 \times 10^{-6}$	$1.20 \times 10^9$	3.81	$1.15 \times 10^{-1}$
7	$1.00 \times 10^{-6}$	$1.50 \times 10^9$	8.90	$8.73 \times 10^{-2}$
7	$1.00 \times 10^{-6}$	$2.00 \times 10^9$	18.6	$4.07 \times 10^{-2}$
7	$1.00 \times 10^{-6}$	$2.50 \times 10^9$	28.7	$2.39 \times 10^{-2}$
7	$1.00 \times 10^{-6}$	$3.00 \times 10^9$	39.7	$1.92 \times 10^{-2}$
7	$1.00 \times 10^{-6}$	$4.00 \times 10^9$	58.5	$1.28 \times 10^{-2}$
7	$1.00 \times 10^{-6}$	$5.00 \times 10^9$	71.9	$1.00 \times 10^{-2}$
7	$1.00 \times 10^{-6}$	$7.00 \times 10^9$	88.0	$7.30 \times 10^{-3}$
7	$1.00 \times 10^{-7}$	$2.15 \times 10^{10}$	16.8	$7.09 \times 10^{-2}$
7	$1.00 \times 10^{-7}$	$2.59 \times 10^{10}$	27.6	$6.90 \times 10^{-2}$
7	$1.00 \times 10^{-7}$	$3.23 \times 10^{10}$	58.4	$3.64 \times 10^{-2}$
7	$1.00 \times 10^{-7}$	$4.31 \times 10^{10}$	16.9	$1.06 \times 10^{-2}$
7	$1.00 \times 10^{-7}$	$5.39 \times 10^{10}$	42.2	$1.05 \times 10^{-2}$
7	$1.00 \times 10^{-7}$	$6.46 \times 10^{10}$	72.9	$4.95 \times 10^{-3}$
7	$1.00 \times 10^{-7}$	$8.62 \times 10^{10}$	77.1	$2.79 \times 10^{-3}$
7	$1.00 \times 10^{-7}$	$1.08 \times 10^{11}$	88.4	$1.24 \times 10^{-3}$
7	$1.00 \times 10^{-7}$	$1.51 \times 10^{11}$	122.0	$9.65 \times 10^{-4}$